Supplement of Geosci. Model Dev., 15, 7243–7255, 2022
https://doi.org/10.5194/gmd-15-7243-2022-supplement

Geoscientific Model Development
Open Access
EGU

Supplement of

Transport parameterization of the Polar SWIFT model (version 2)

Ingo Wohltmann et al.

Correspondence to: Ingo Wohltmann (ingo.wohltmann@awi.de)

1 Observed change (northern hemisphere)

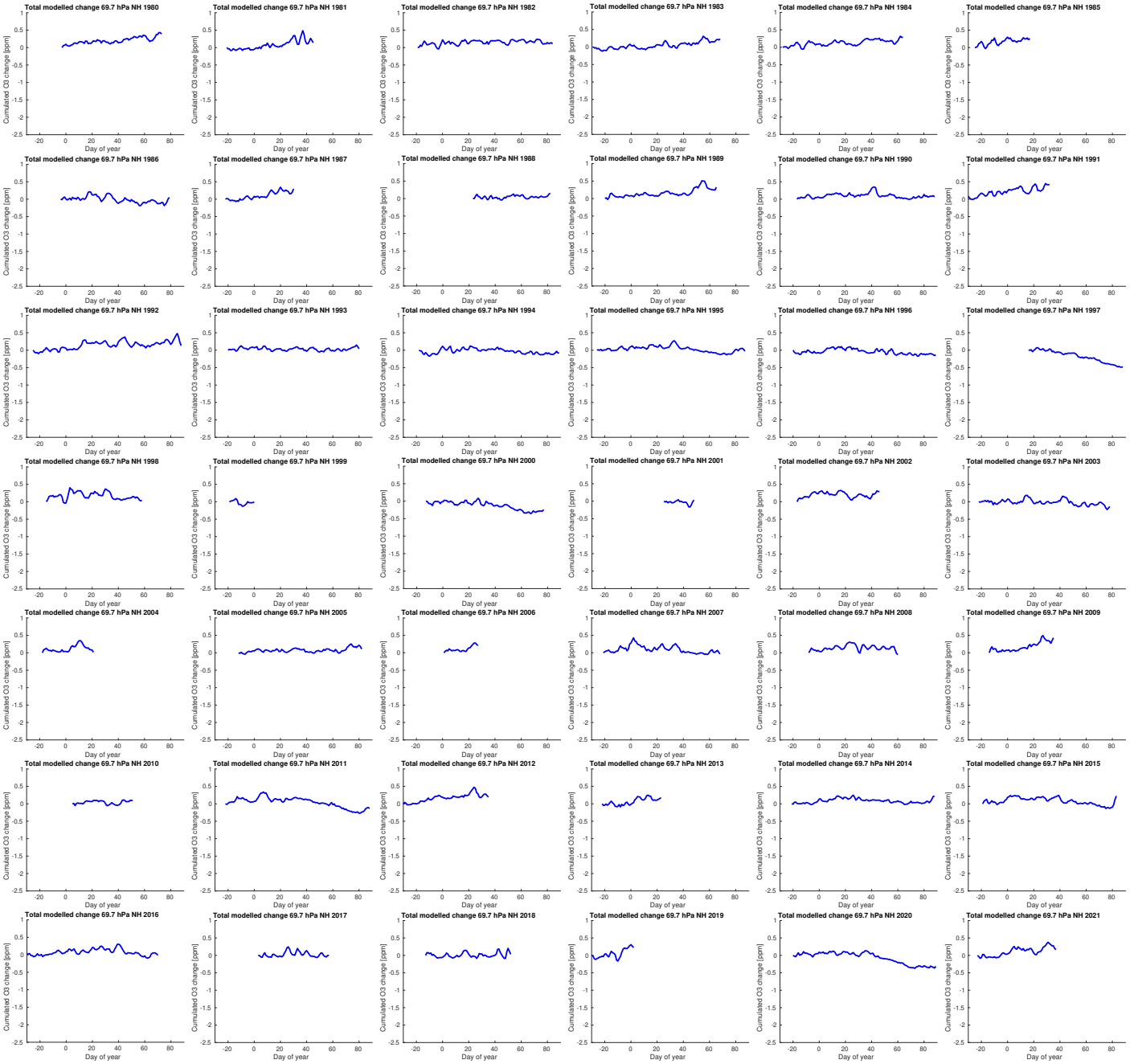

Figure S1: Cumulated total change of vortex-averaged ozone mixing ratio for the northern hemispheric winters 1979/1980–2020/2021 at 70 hPa (layer 1) simulated by ATLAS-SWIFT as a function of the day of year (cf. Figure 1a of the main manuscript).

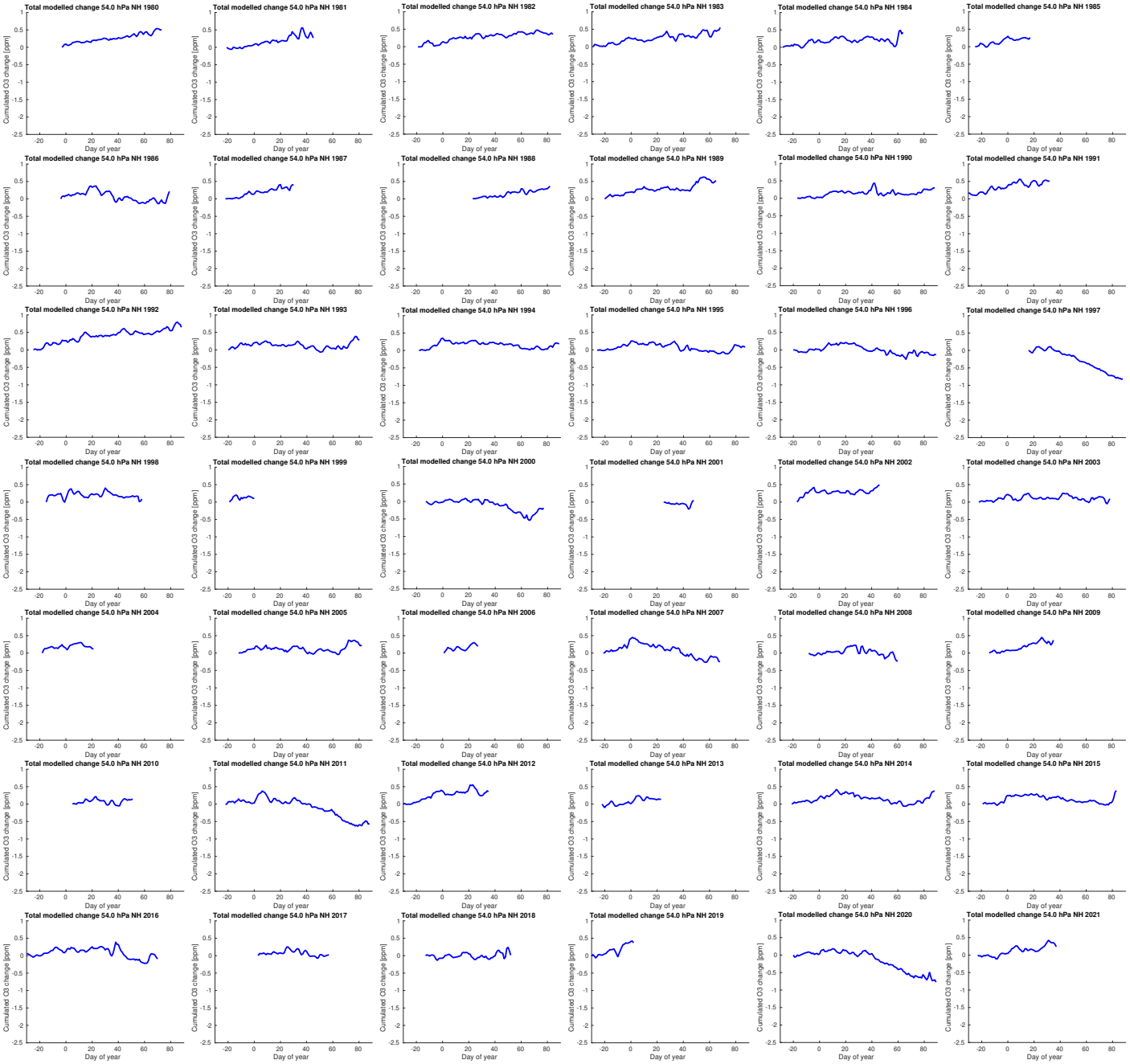

Figure S2: Cumulated total change of vortex-averaged ozone mixing ratio for the northern hemispheric winters 1979/1980–2020/2021 at 54 hPa (layer 2) simulated by ATLAS-SWIFT as a function of the day of year (cf. Figure 1a of the main manuscript).

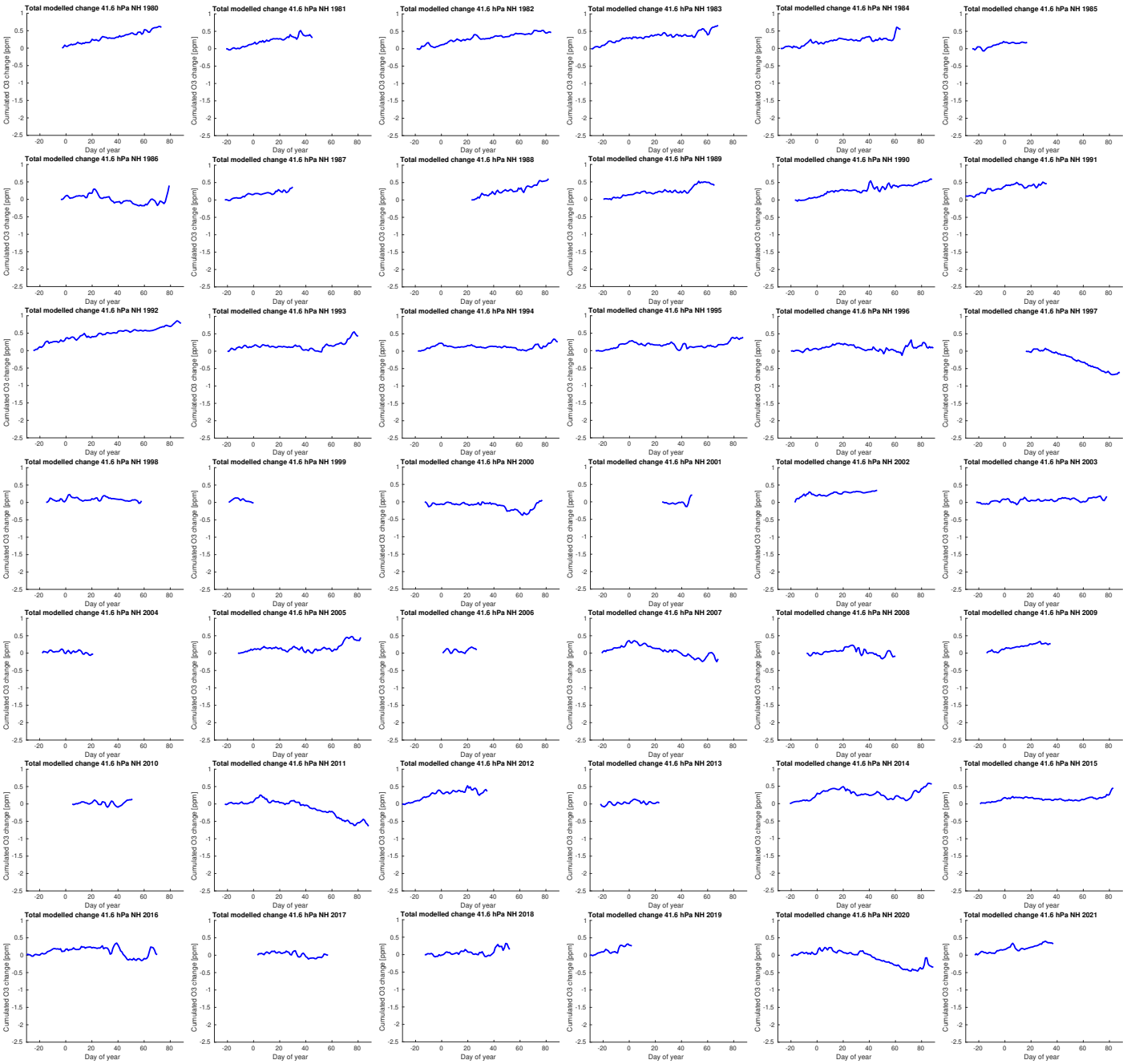

Figure S3: Cumulated total change of vortex-averaged ozone mixing ratio for the northern hemispheric winters 1979/1980–2020/2021 at 42 hPa (layer 3) simulated by ATLAS-SWIFT as a function of the day of year (cf. Figure 1a of the main manuscript).

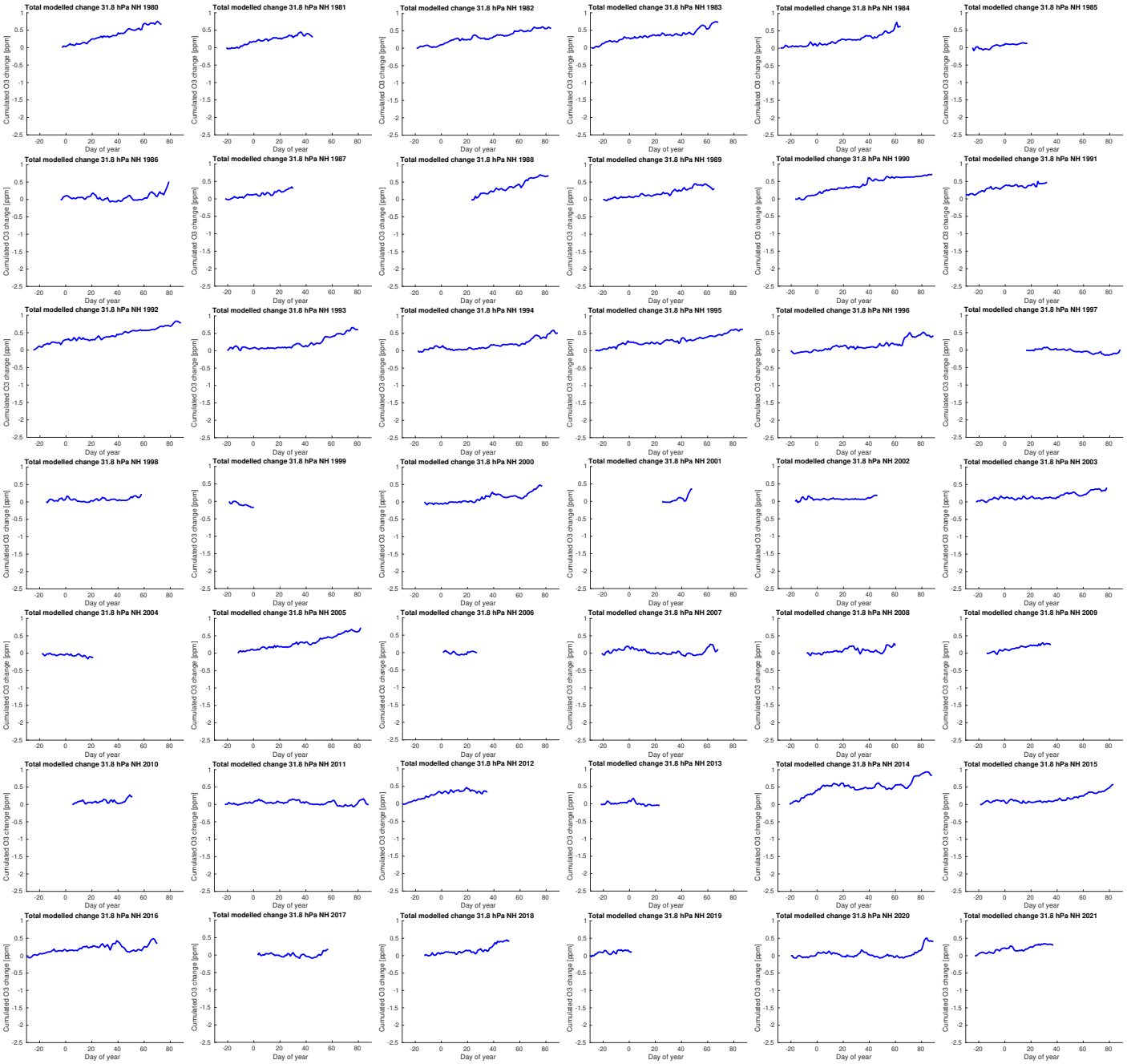

Figure S4: Cumulated total change of vortex-averaged ozone mixing ratio for the northern hemispheric winters 1979/1980–2020/2021 at 32 hPa (layer 4) simulated by ATLAS-SWIFT as a function of the day of year (cf. Figure 1a of the main manuscript).

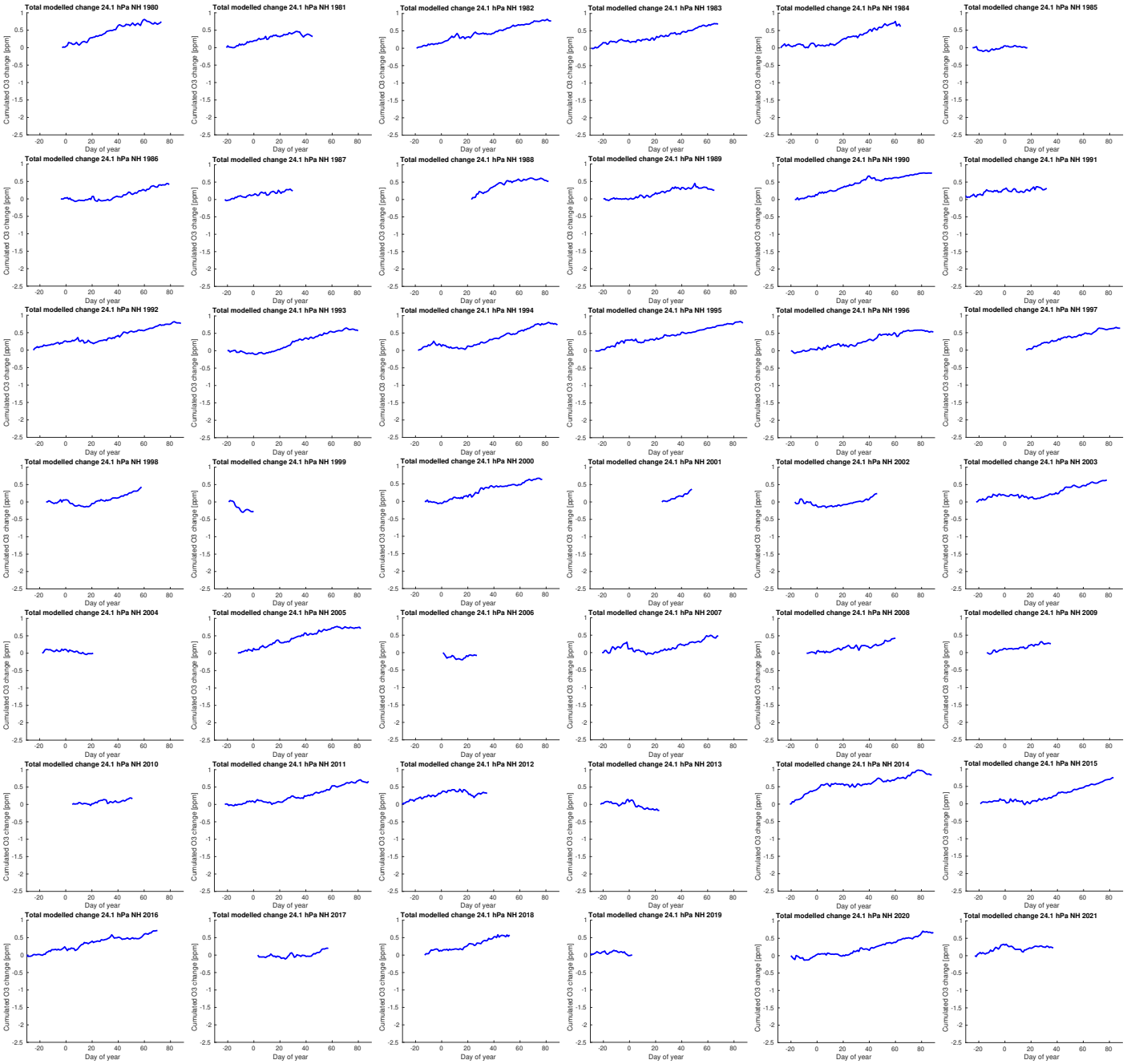

Figure S5: Cumulated total change of vortex-averaged ozone mixing ratio for the northern hemispheric winters 1979/1980–2020/2021 at 24 hPa (layer 5) simulated by ATLAS-SWIFT as a function of the day of year (cf. Figure 1a of the main manuscript).

2 Chemical change (northern hemisphere)

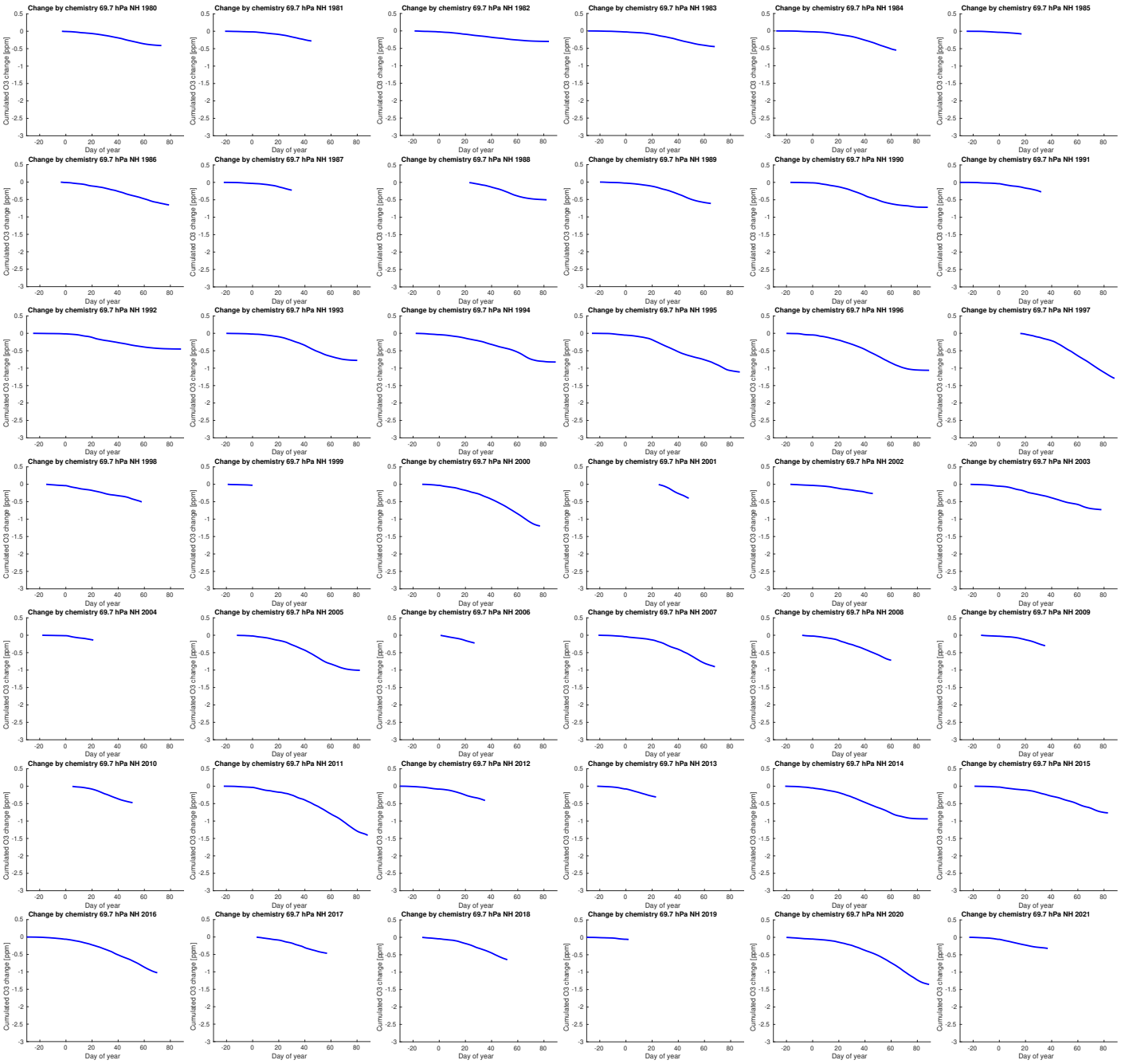

Figure S6: Cumulated change by chemistry of vortex-averaged ozone mixing ratio for the northern hemispheric winters 1979/1980–2020/2021 at 70 hPa (layer 1) simulated by ATLAS-SWIFT as a function of the day of year (cf. Figure 1c of the main manuscript).

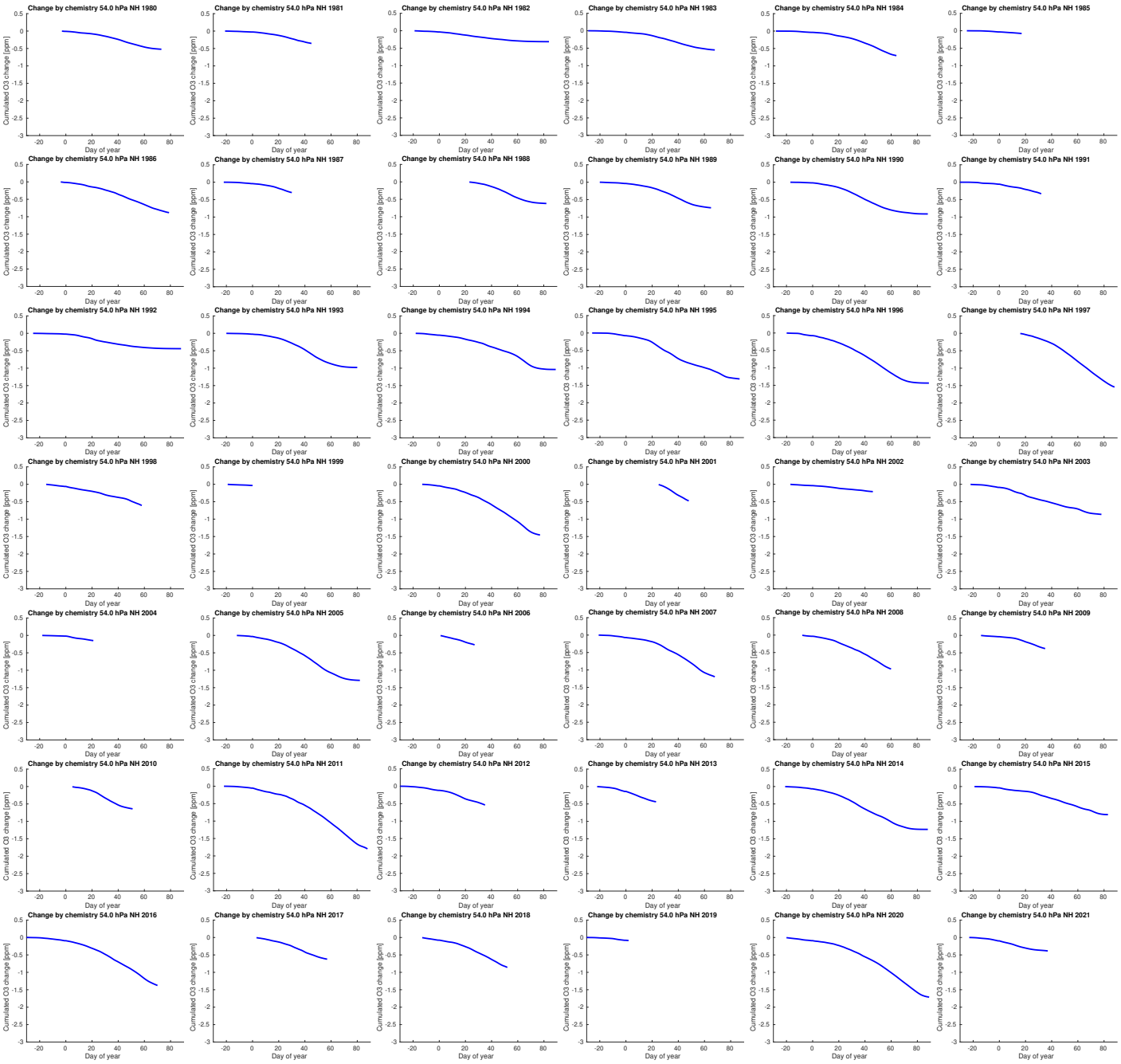

Figure S7: Cumulated change by chemistry of vortex-averaged ozone mixing ratio for the northern hemispheric winters 1979/1980–2020/2021 at 54 hPa (layer 2) simulated by ATLAS-SWIFT as a function of the day of year (cf. Figure 1c of the main manuscript).

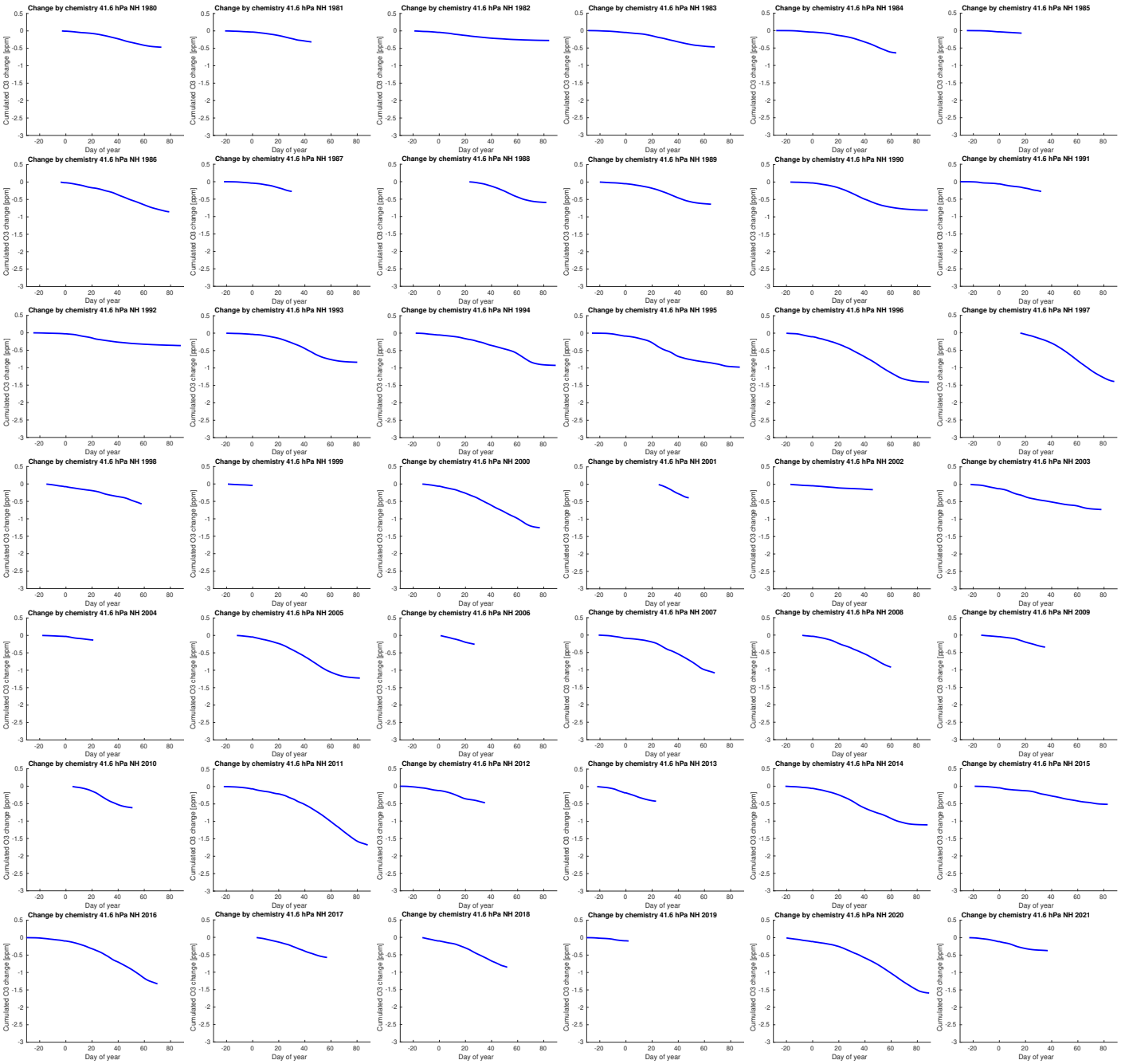

Figure S8: Cumulated change by chemistry of vortex-averaged ozone mixing ratio for the northern hemispheric winters 1979/1980–2020/2021 at 42 hPa (layer 3) simulated by ATLAS-SWIFT as a function of the day of year (cf. Figure 1c of the main manuscript).

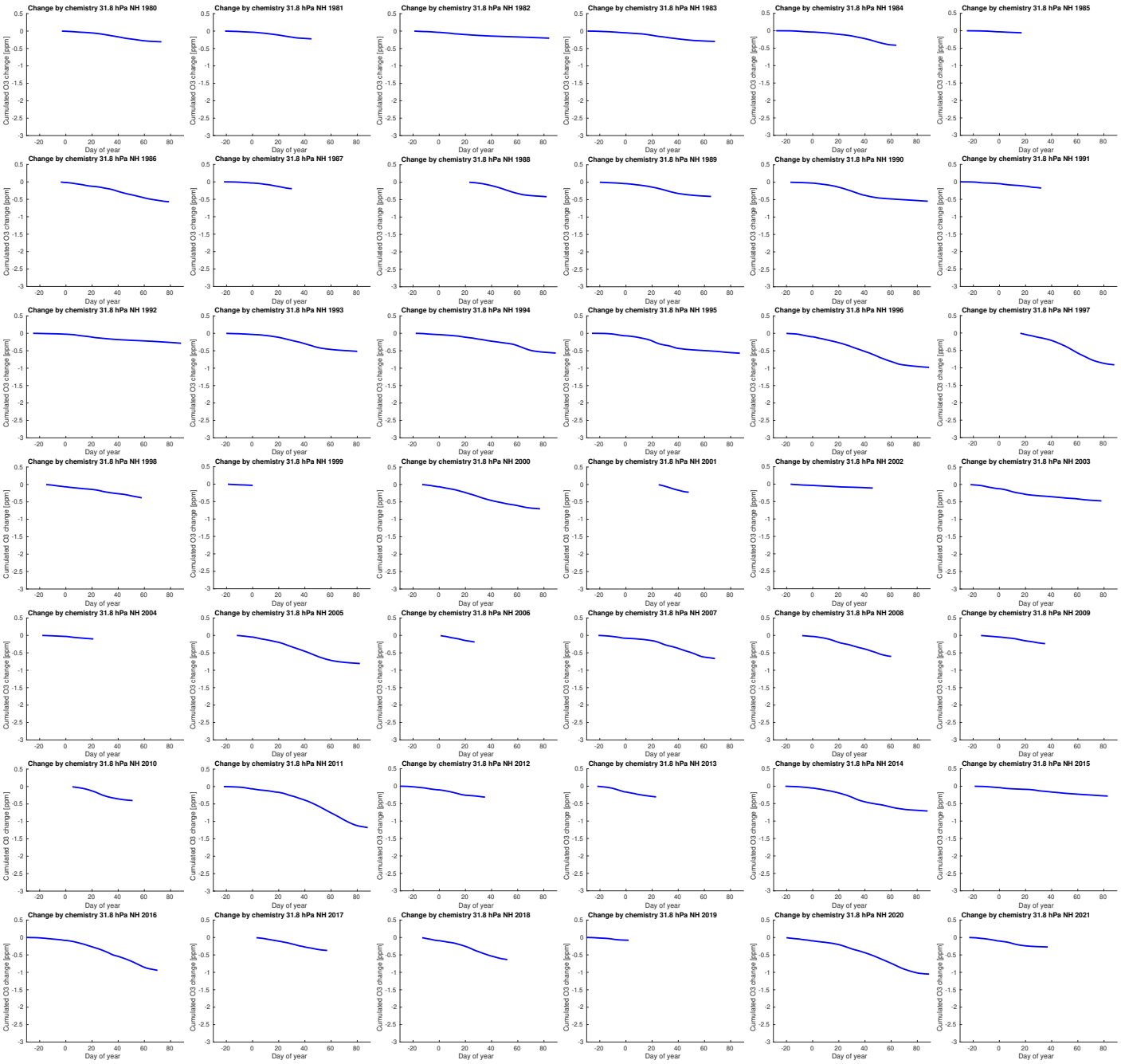

Figure S9: Cumulated change by chemistry of vortex-averaged ozone mixing ratio for the northern hemispheric winters 1979/1980–2020/2021 at 32 hPa (layer 4) simulated by ATLAS-SWIFT as a function of the day of year (cf. Figure 1c of the main manuscript).

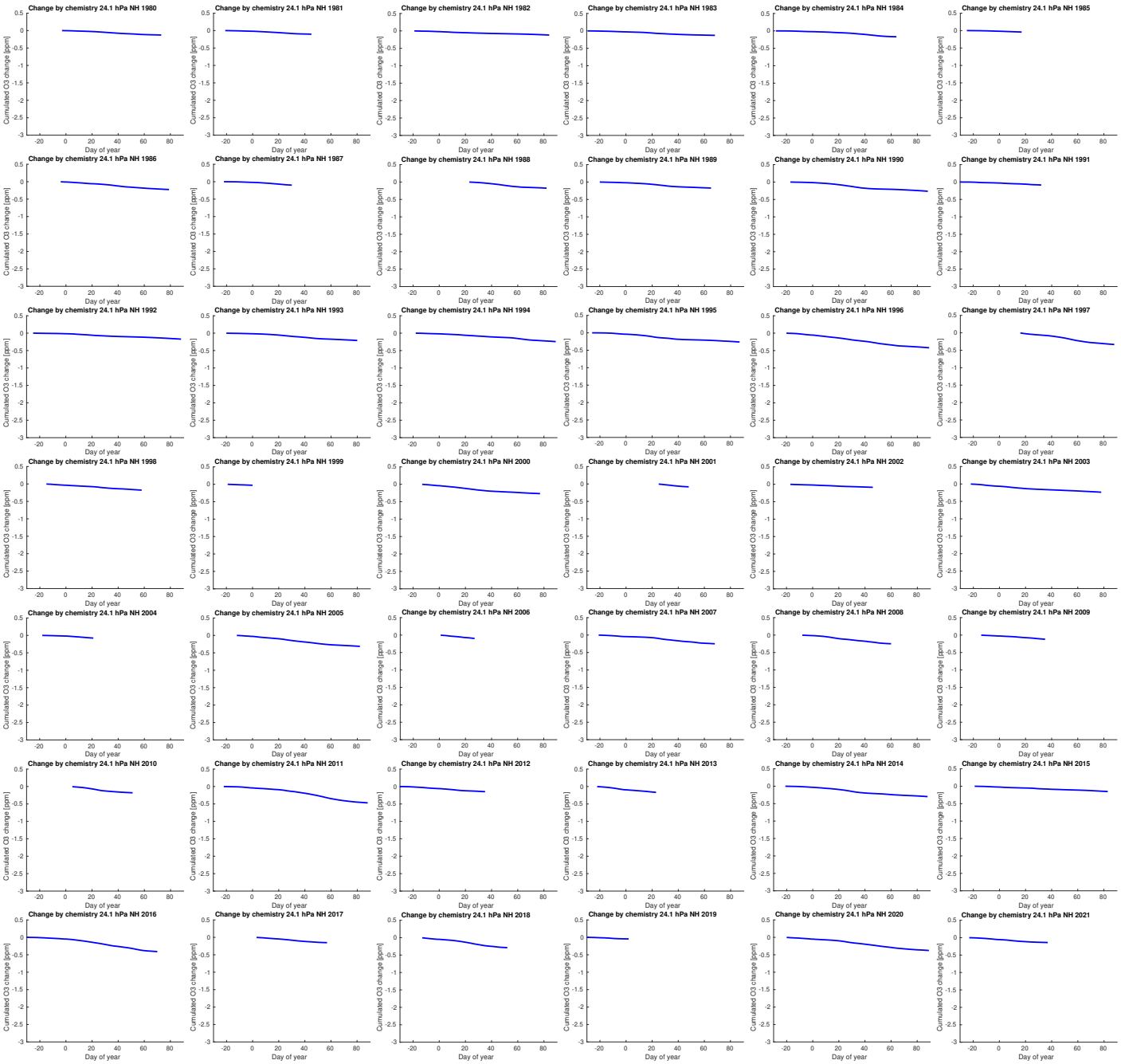

Figure S10: Cumulated change by chemistry of vortex-averaged ozone mixing ratio for the northern hemispheric winters 1979/1980–2020/2021 at 24 hPa (layer 5) simulated by ATLAS-SWIFT as a function of the day of year (cf. Figure 1c of the main manuscript).

3 Transport change (northern hemisphere)

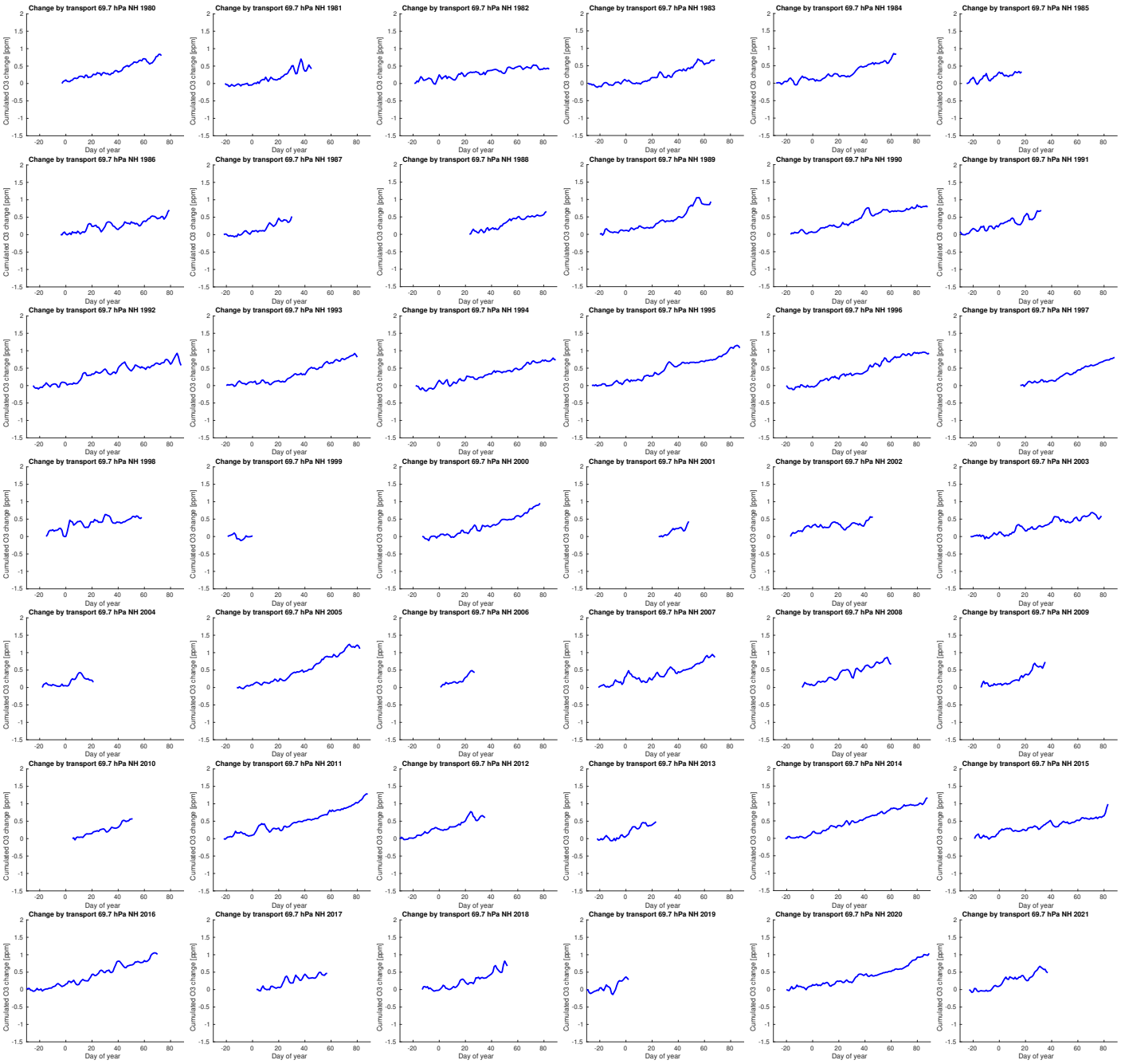

Figure S11: Cumulated change by transport of vortex-averaged ozone mixing ratio for the northern hemispheric winters 1979/1980–2020/2021 at 70 hPa (layer 1) simulated by ATLAS-SWIFT as a function of the day of year (cf. Figure 1e of the main manuscript).

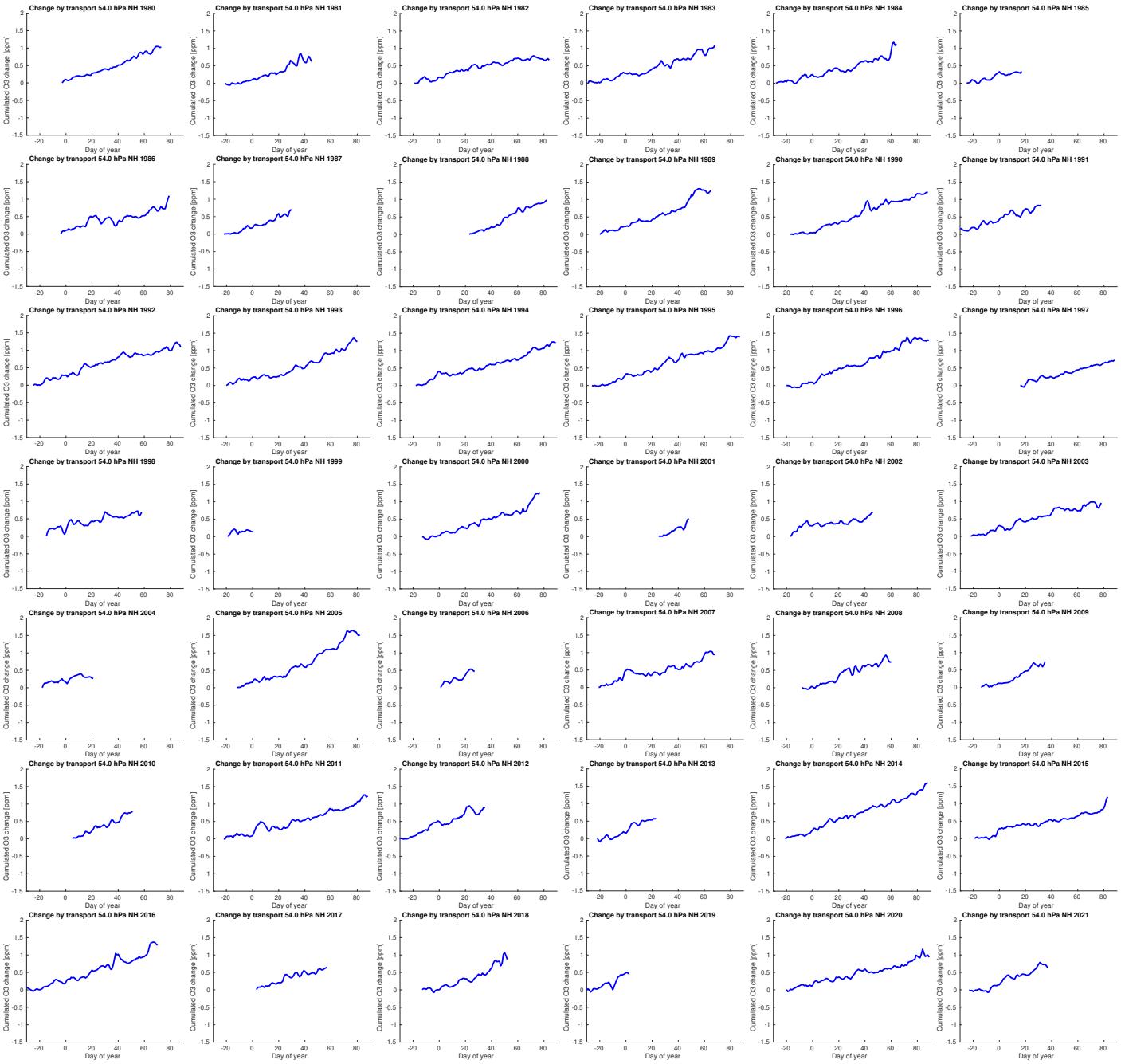

Figure S12: Cumulated change by transport of vortex-averaged ozone mixing ratio for the northern hemispheric winters 1979/1980–2020/2021 at 54 hPa (layer 2) simulated by ATLAS-SWIFT as a function of the day of year (cf. Figure 1e of the main manuscript).

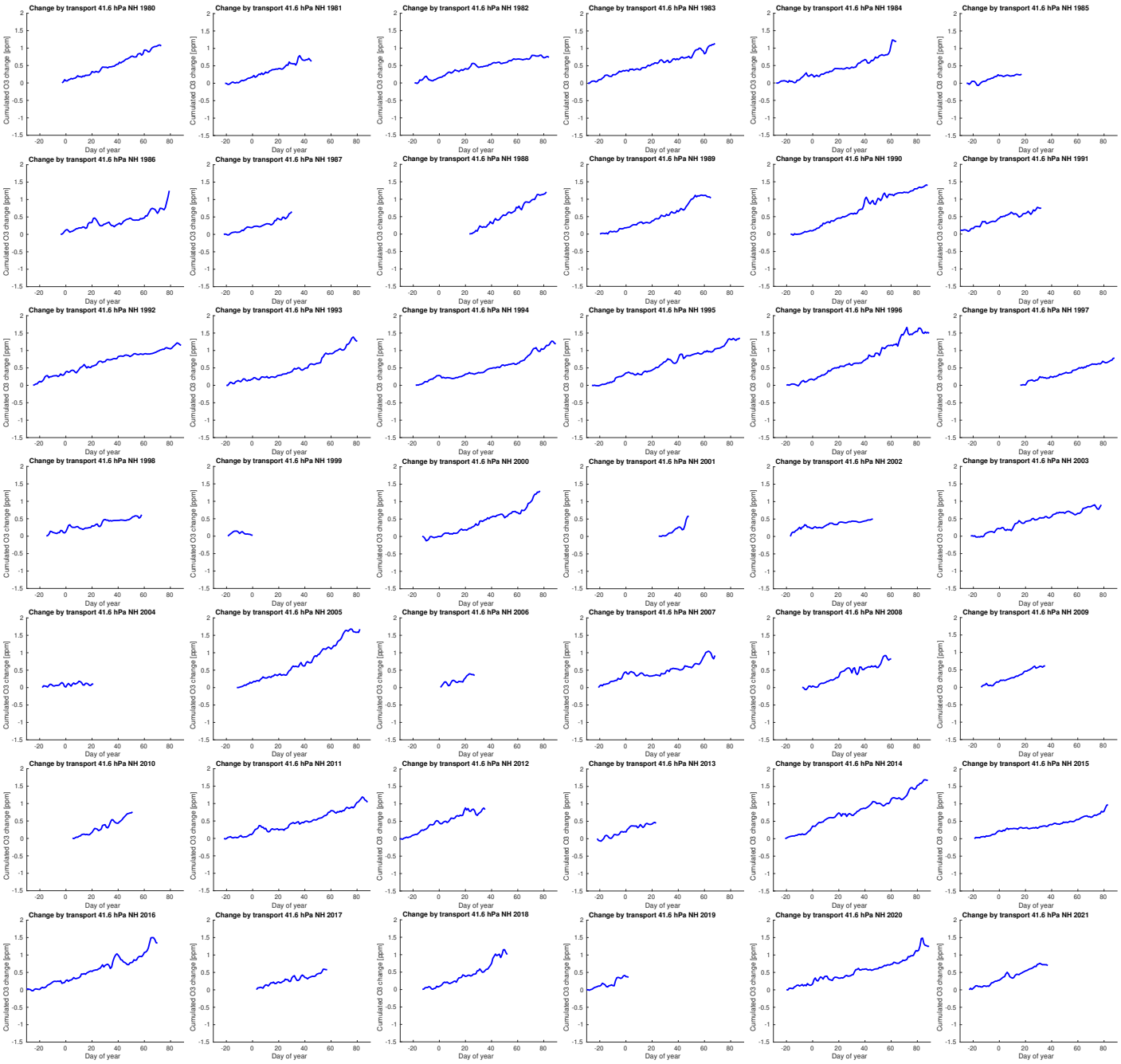

Figure S13: Cumulated change by transport of vortex-averaged ozone mixing ratio for the northern hemispheric winters 1979/1980–2020/2021 at 42 hPa (layer 3) simulated by ATLAS-SWIFT as a function of the day of year (cf. Figure 1e of the main manuscript).

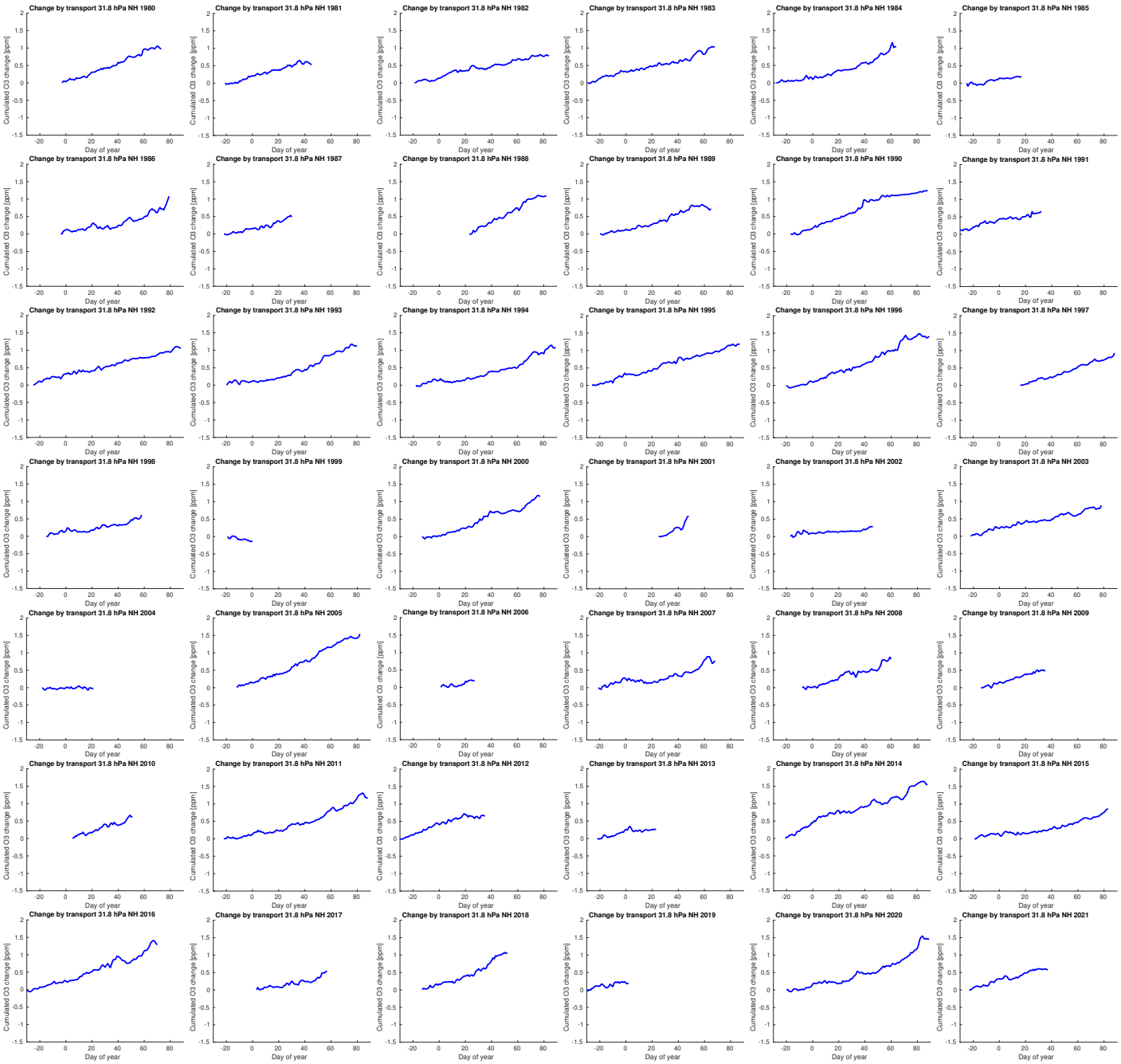

Figure S14: Cumulated change by transport of vortex-averaged ozone mixing ratio for the northern hemispheric winters 1979/1980–2020/2021 at 32 hPa (layer 4) simulated by ATLAS-SWIFT as a function of the day of year (cf. Figure 1e of the main manuscript).

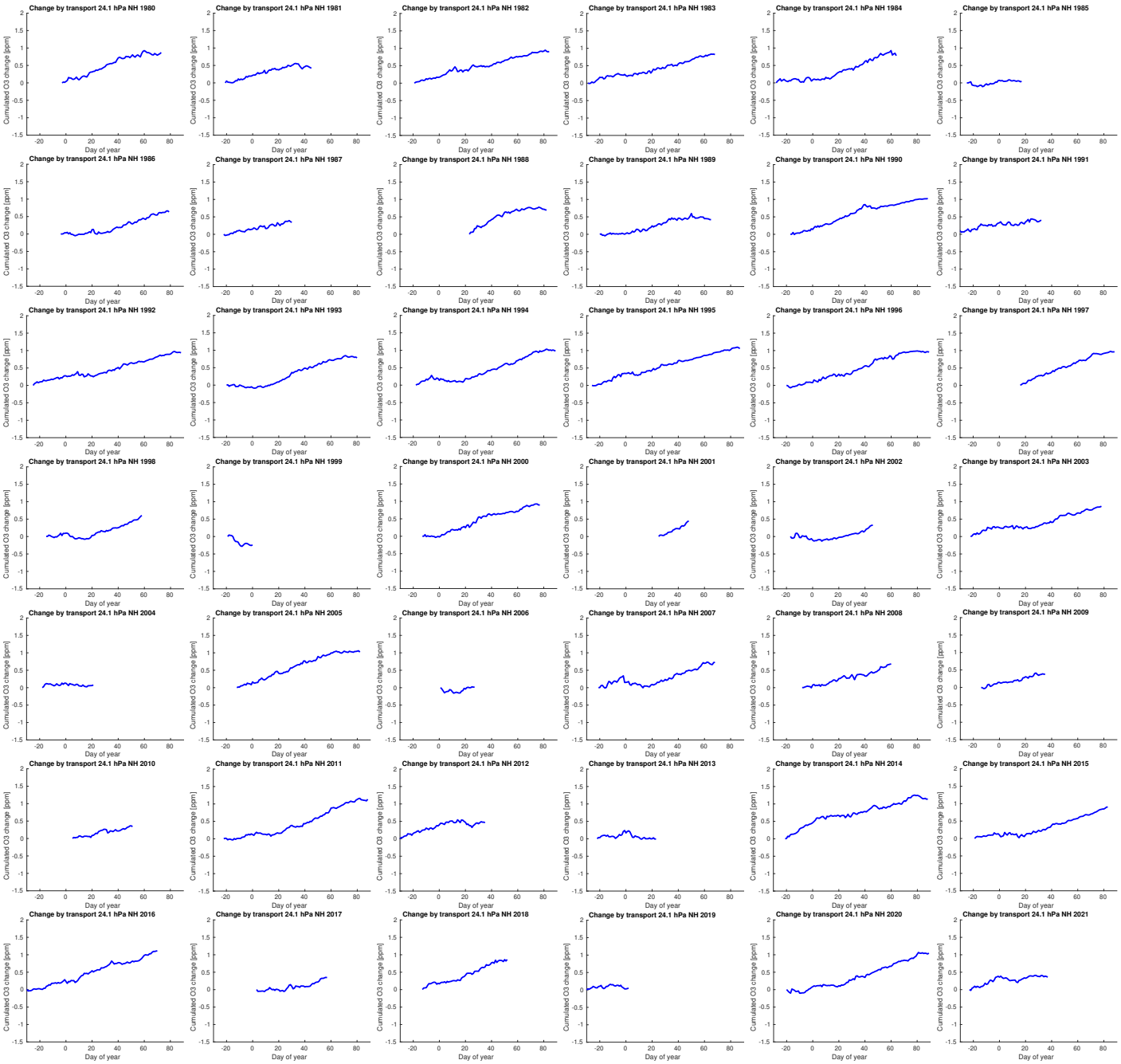

Figure S15: Cumulated change by transport of vortex-averaged ozone mixing ratio for the northern hemispheric winters 1979/1980–2020/2021 at 24 hPa (layer 5) simulated by ATLAS-SWIFT as a function of the day of year (cf. Figure 1e of the main manuscript).

4 Fit (northern hemisphere)

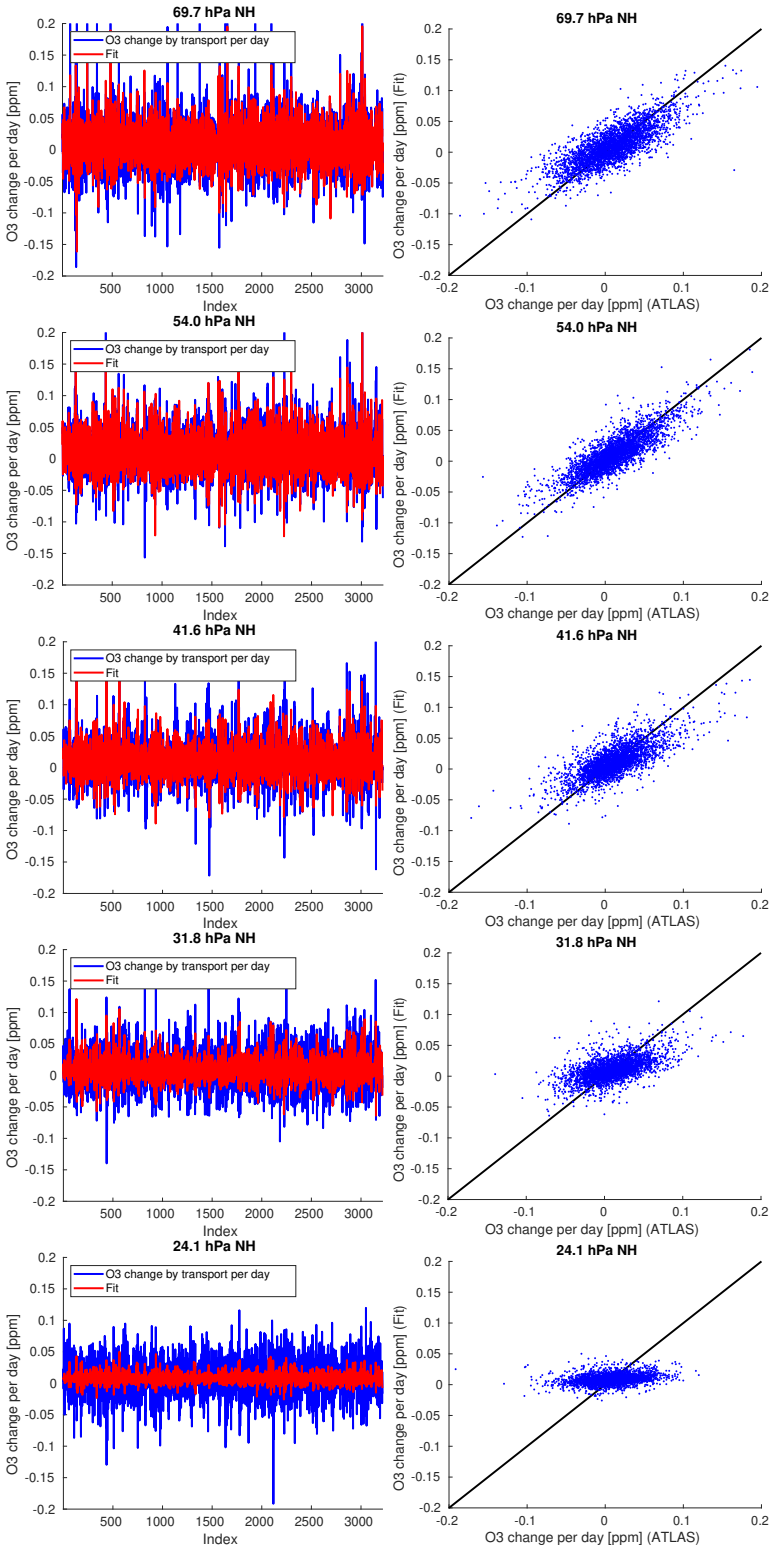

Figure S16: Left (cf. Figure 2a of the main manuscript): Concatenated time series of the change of vortex-averaged ozone mixing ratio by transport per day for all years in ATLAS-SWIFT (blue) and corresponding fit from the multivariate regression model (red). Right (cf. Figure 2c of the main manuscript): Same data as a scatter plot.

5 Vortex mean temperatures (northern hemisphere)

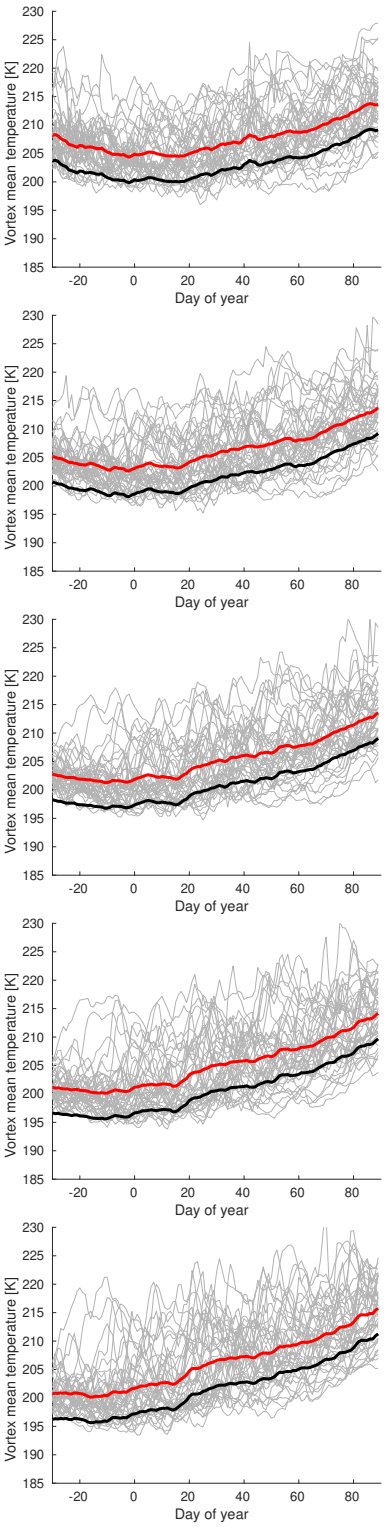

Figure S17: Vortex mean temperatures at the SWIFT levels as a function of day of year for all individual years from 1979/1980 to 2020/2021 based on ERA5 (grey lines), vortex mean temperature averaged over all years (red) and the same curve shifted by $-4.5\,\mathrm{K}$ as an approximation of the lower envelope of the grey lines (black) (cf. Figure 3a of the main manuscript).

6 Change of ozone versus change of temperature (northern hemisphere)

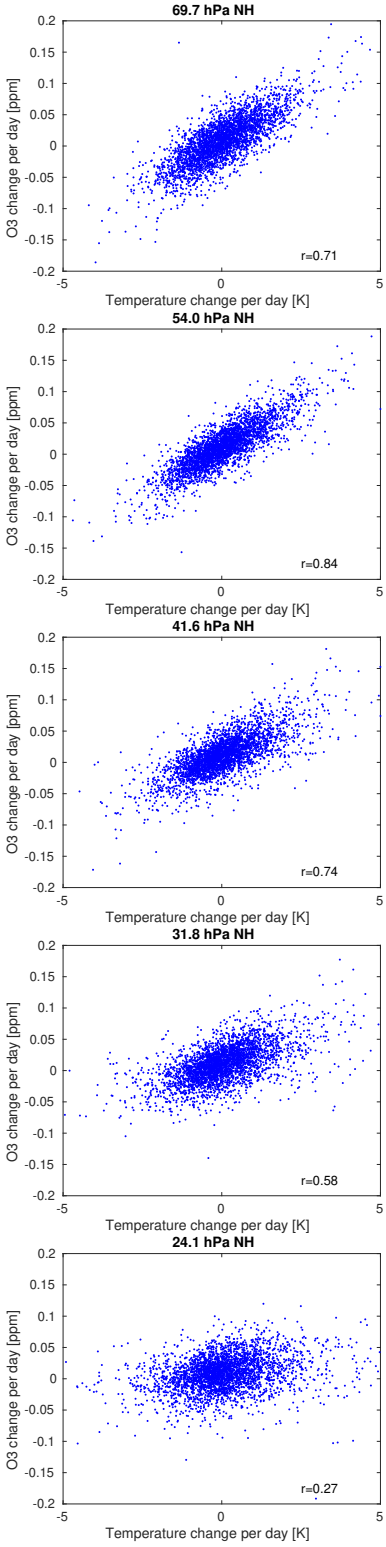

Figure S18: Scatter plot of the change of vortex-averaged ozone mixing ratio by transport per day for all years in ATLAS-SWIFT and corresponding change in vortex-averaged temperature per day, corrected for the change in radiative equilibrium temperature (cf. Figure 4a of the main manuscript).

7 Validation of the transport term (northern hemisphere)

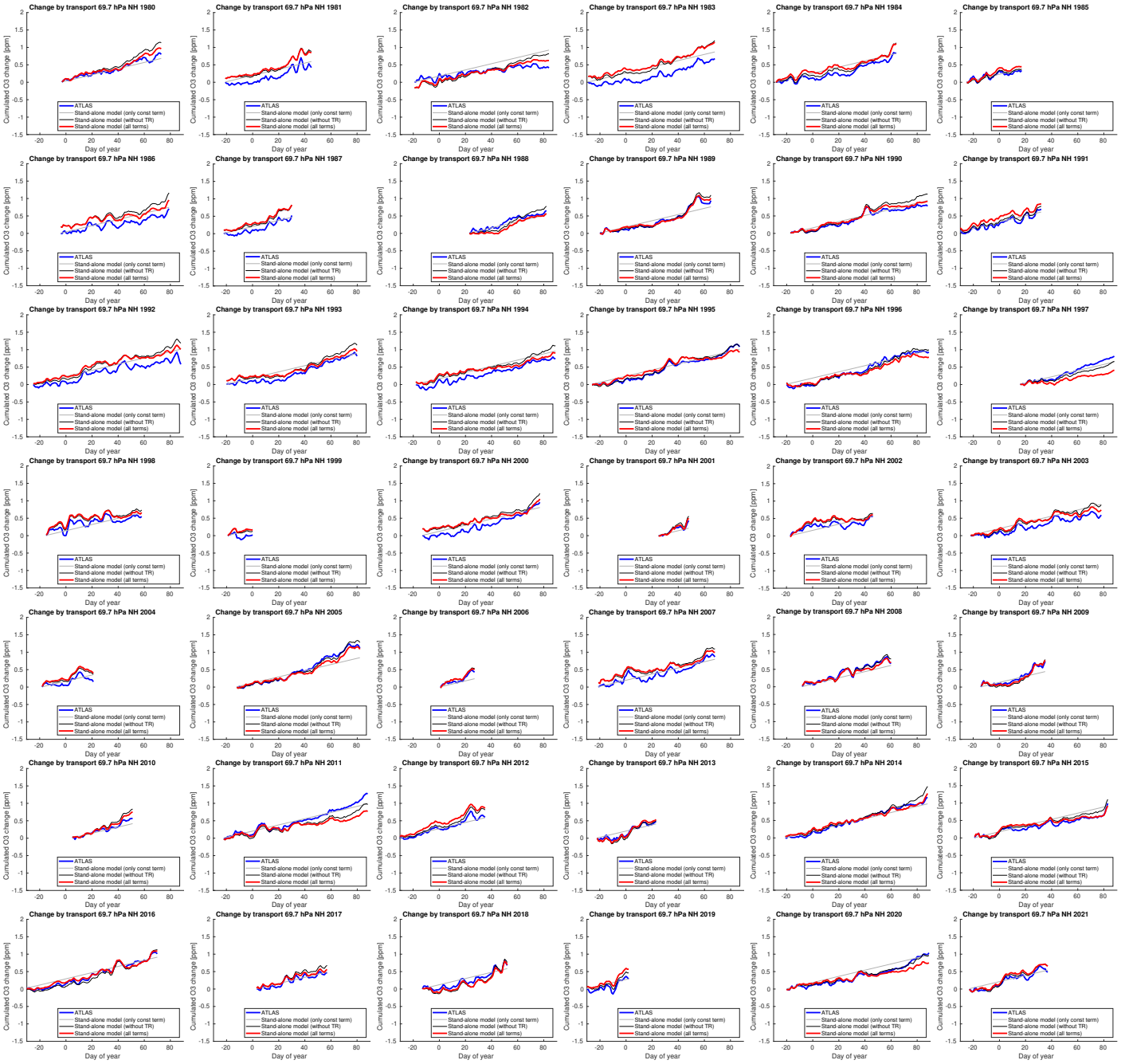

Figure S19: Cumulated vortex-averaged ozone change by transport at 70 hPa (layer 1) for the northern hemispheric winters 1979/1980–2020/2021 (blue) and a simulation of the cumulated change by transport by a stand-alone version of the transport parameterization (red). The thin grey line shows a simulation with only the constant term, and the thin black line shows a simulation with the constant and temperature-dependent term, but without subtracting the change of the radiative equilibrium temperature from the vortex-averaged temperature change (cf. Figure 5a of the main manuscript).

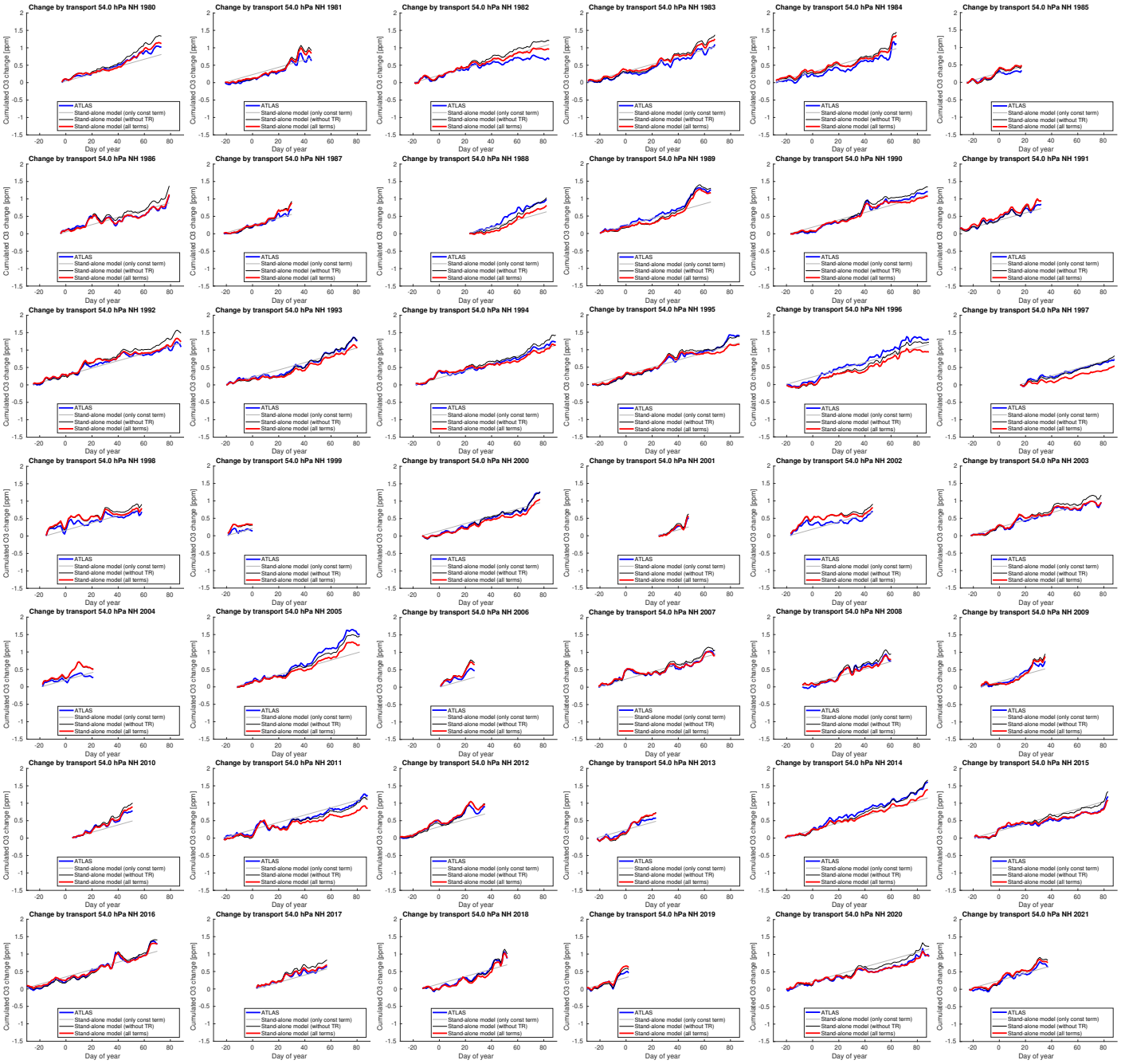

Figure S20: Cumulated vortex-averaged ozone change by transport at 54 hPa (layer 2) for the northern hemispheric winters 1979/1980–2020/2021 (blue) and a simulation of the cumulated change by transport by a stand-alone version of the transport parameterization (red). The thin grey line shows a simulation with only the constant term, and the thin black line shows a simulation with the constant and temperature-dependent term, but without subtracting the change of the radiative equilibrium temperature from the vortex-averaged temperature change (cf. Figure 5a of the main manuscript).

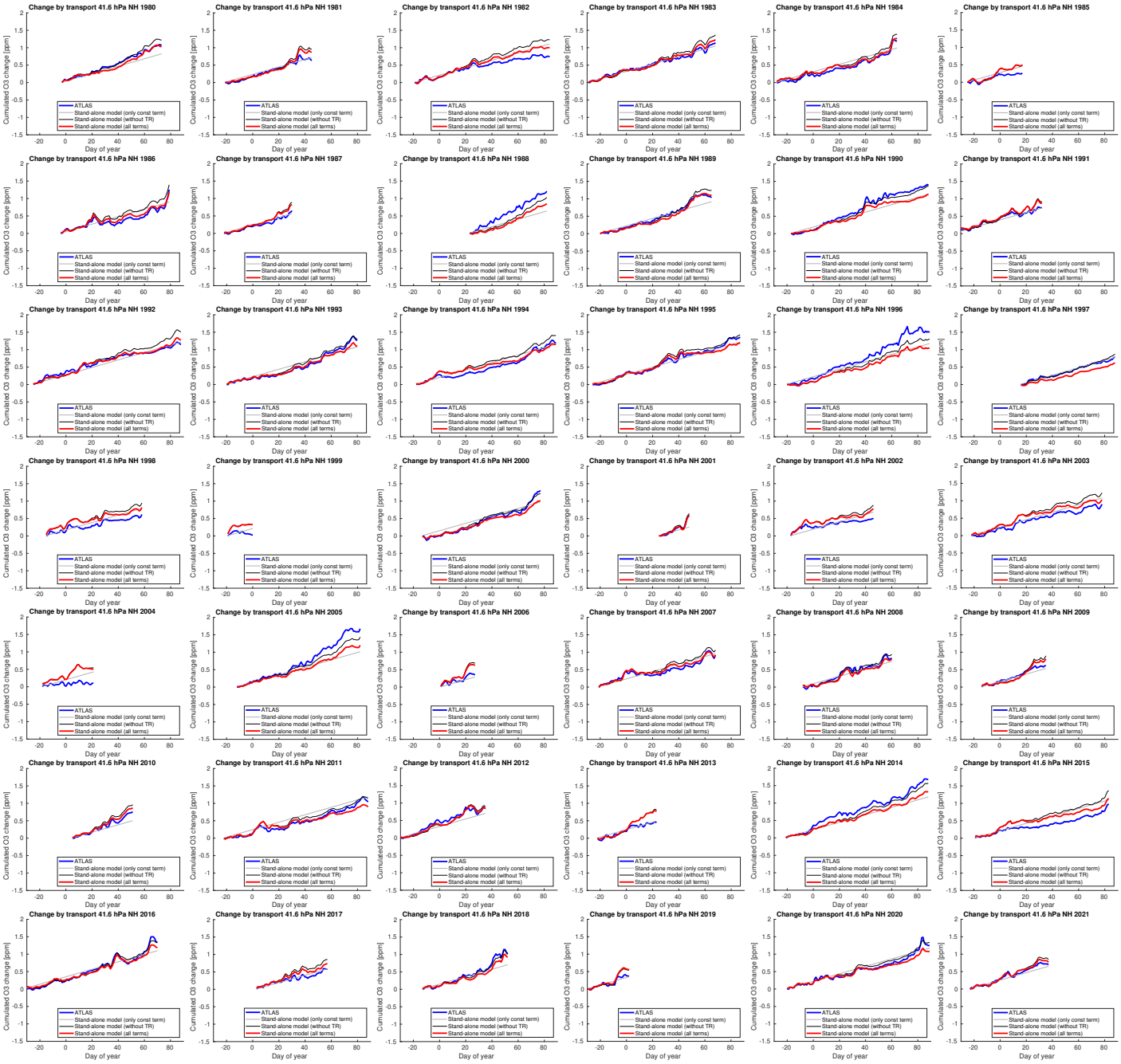

Figure S21: Cumulated vortex-averaged ozone change by transport at 42 hPa (layer 3) for the northern hemispheric winters 1979/1980–2020/2021 (blue) and a simulation of the cumulated change by transport by a stand-alone version of the transport parameterization (red). The thin grey line shows a simulation with only the constant term, and the thin black line shows a simulation with the constant and temperature-dependent term, but without subtracting the change of the radiative equilibrium temperature from the vortex-averaged temperature change (cf. Figure 5a of the main manuscript).

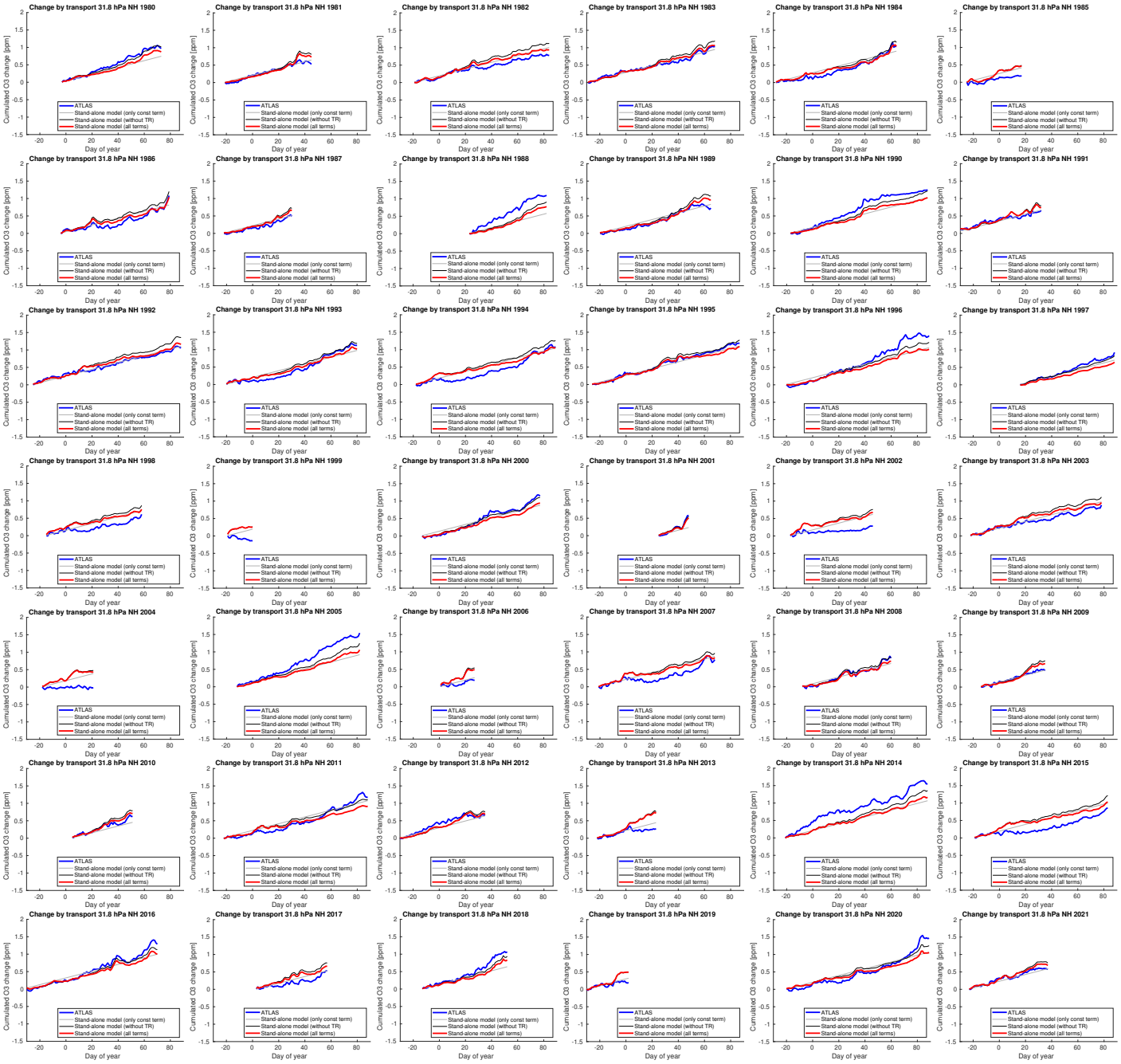

Figure S22: Cumulated vortex-averaged ozone change by transport at 32 hPa (layer 4) for the northern hemispheric winters 1979/1980–2020/2021 (blue) and a simulation of the cumulated change by transport by a stand-alone version of the transport parameterization (red). The thin grey line shows a simulation with only the constant term, and the thin black line shows a simulation with the constant and temperature-dependent term, but without subtracting the change of the radiative equilibrium temperature from the vortex-averaged temperature change (cf. Figure 5a of the main manuscript).

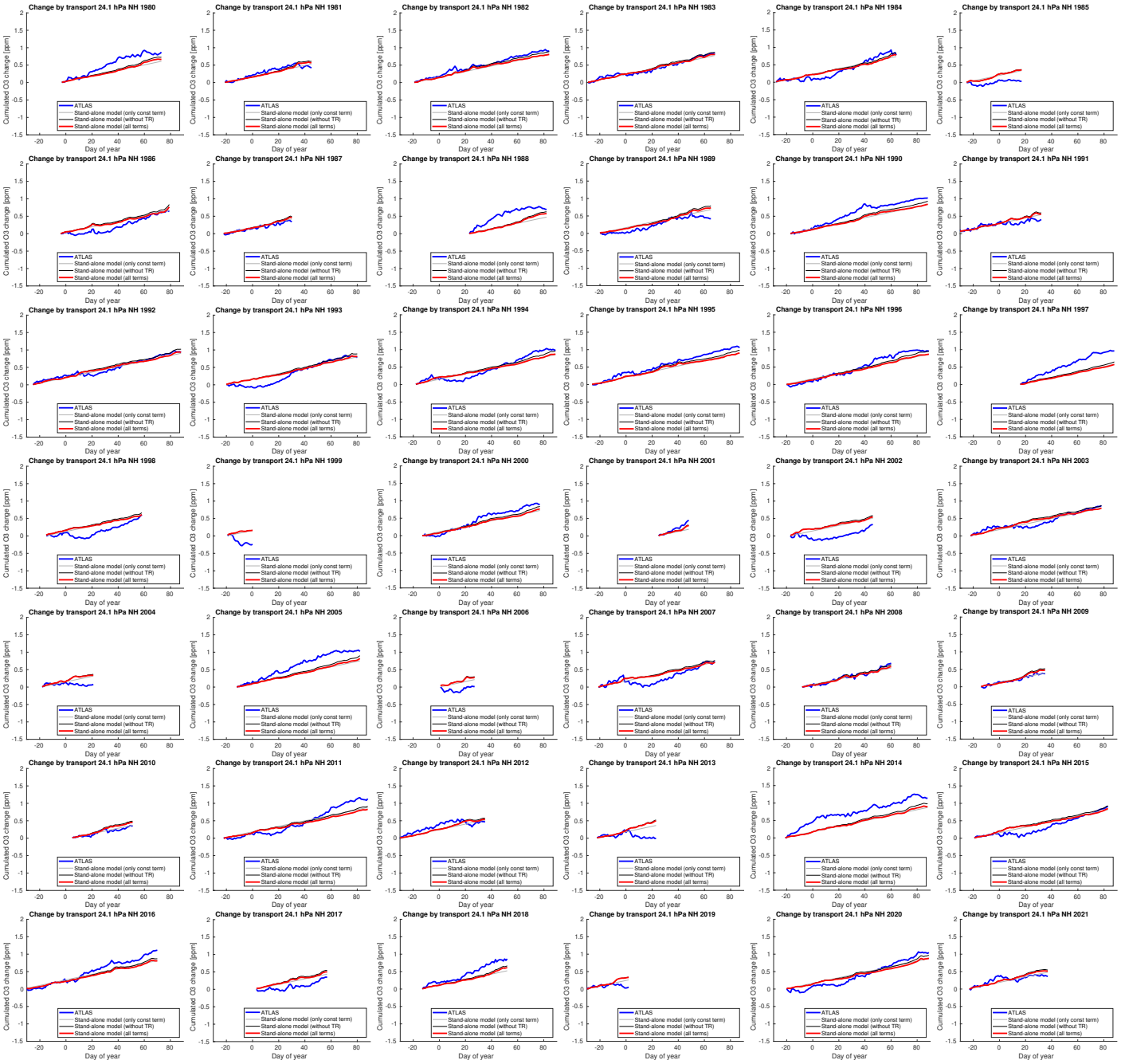

Figure S23: Cumulated vortex-averaged ozone change by transport at 24 hPa (layer 5) for the northern hemispheric winters 1979/1980–2020/2021 (blue) and a simulation of the cumulated change by transport by a stand-alone version of the transport parameterization (red). The thin grey line shows a simulation with only the constant term, and the thin black line shows a simulation with the constant and temperature-dependent term, but without subtracting the change of the radiative equilibrium temperature from the vortex-averaged temperature change (cf. Figure 5a of the main manuscript).

8 Validation of the complete SWIFT model (northern hemisphere)

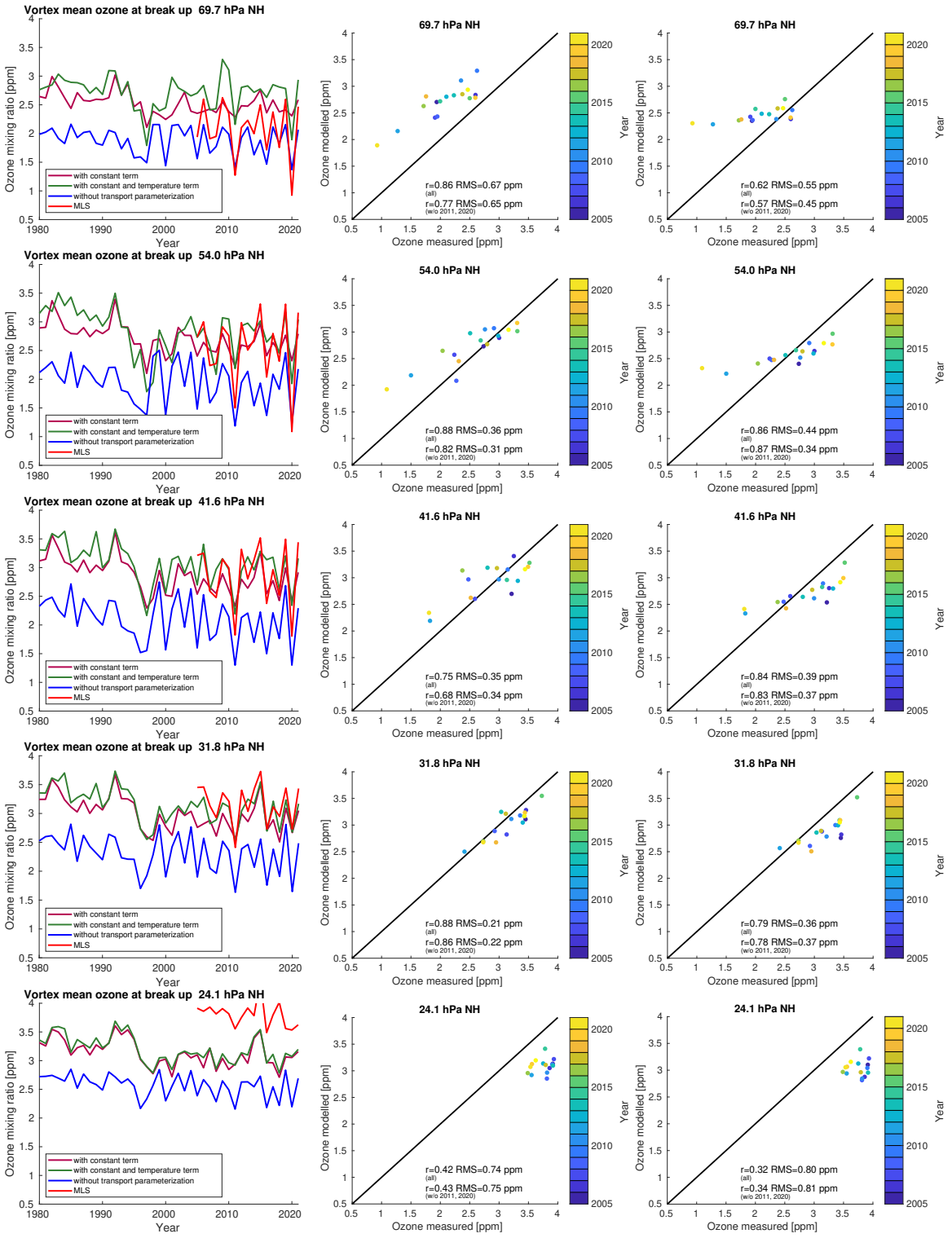

Figure S24: Left (cf. Figure 6a of the main manuscript): Vortex-averaged ozone simulated by the stand-alone Polar SWIFT model for the date of vortex breakup in the northern hemisphere for different years. Ozone mixing ratios simulated without the transport parameterization (blue), ozone mixing ratios simulated with only the "constant change" term of the transport parameterization (brown), ozone mixing ratios simulated with the full transport parameterization with the "constant change" term and temperature-dependent term (green), and corresponding measurements of ozone from the MLS instrument (red). Middle (cf. Figure 7a of the main manuscript): Scatter plot of the same data ("constant change" term and temperature-dependent term). Right: Scatter plot of the same data (only "constant change" term).

9 Difference transport term at vortex breakup of transport parameterization to ATLAS (northern hemisphere)

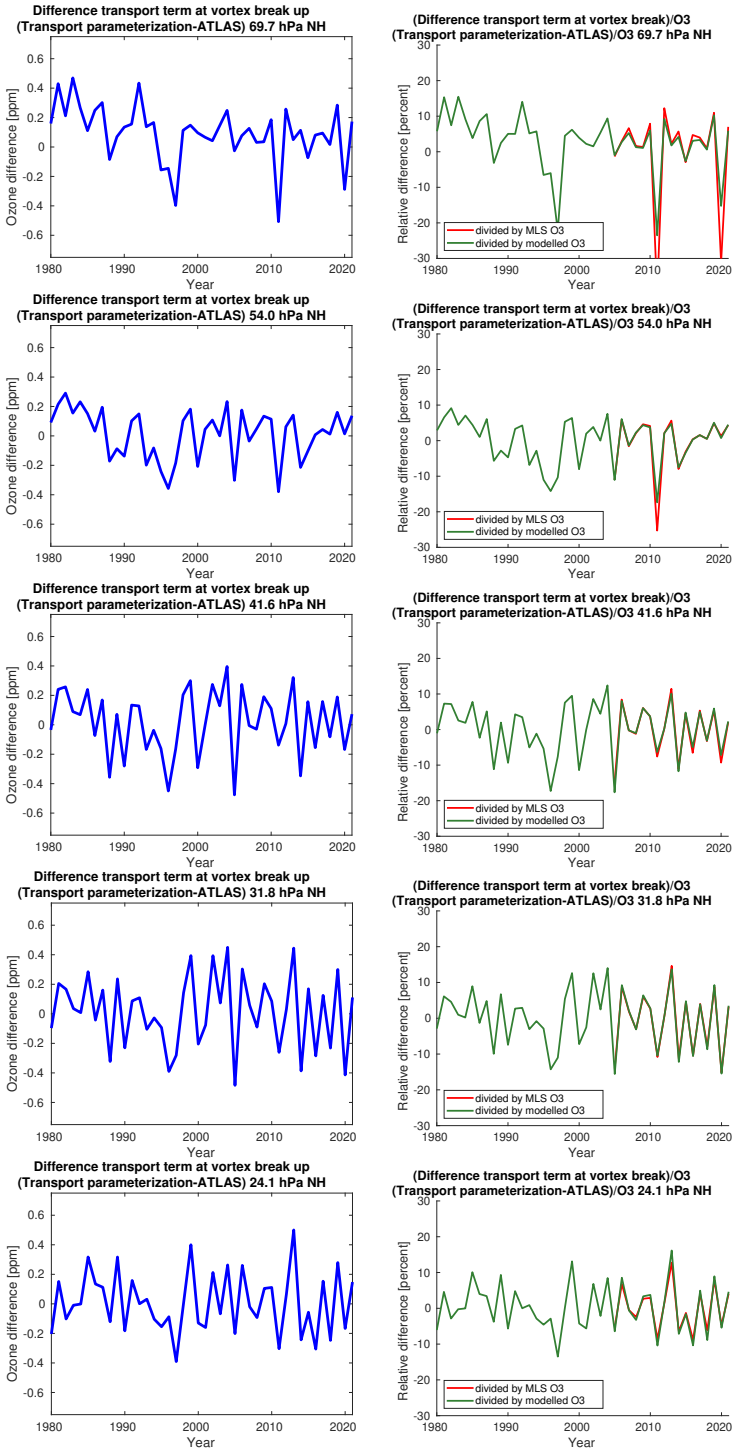

Figure S25: Left: Difference of cumulated vortex-averaged ozone change by transport at vortex break up between the transport parameterization and ATLAS-SWIFT for the northern hemispheric winters 1979/1980–2020/2021. Right: The difference from the left column divided by the ozone that is simulated (green) or observed by MLS (red) at this day.

10 Observed change (southern hemisphere)

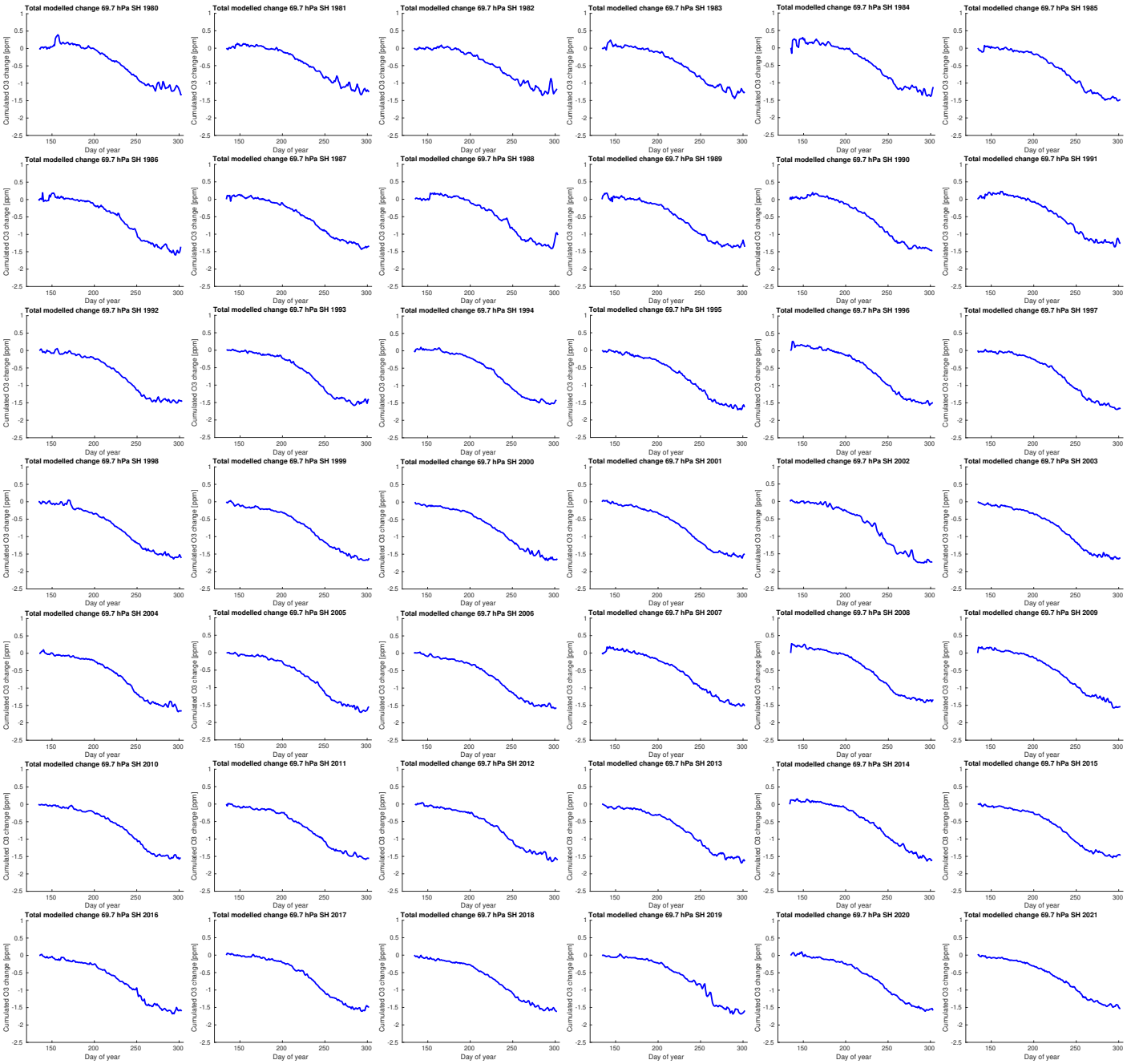

Figure S26: Cumulated total change of vortex-averaged ozone mixing ratio for the southern hemispheric winters 1980–2021 at 70 hPa (layer 1) simulated by ATLAS-SWIFT as a function of the day of year (cf. Figure 1b of the main manuscript).

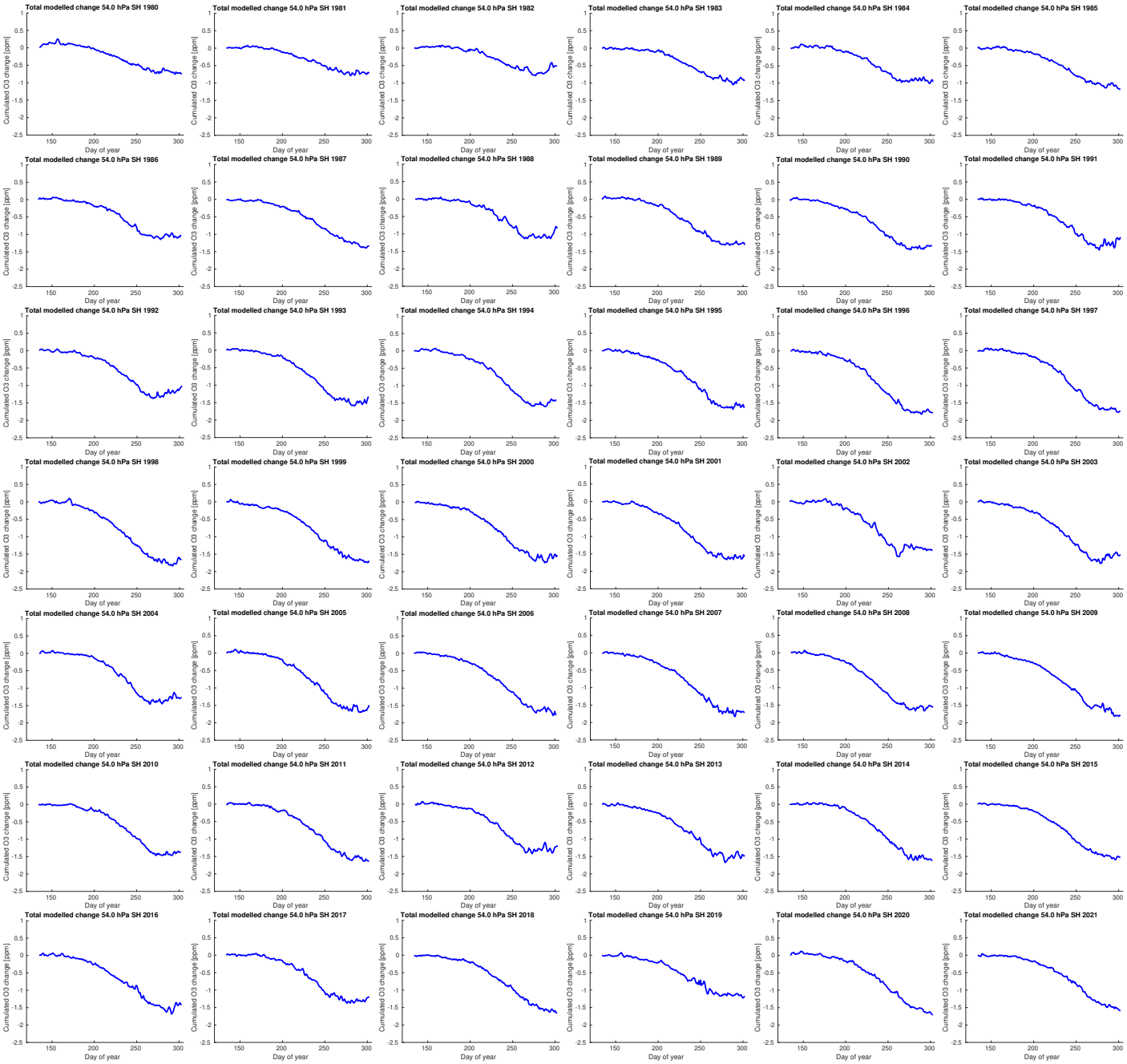

Figure S27: Cumulated total change of vortex-averaged ozone mixing ratio for the southern hemispheric winters 1980–2021 at 54 hPa (layer 2) simulated by ATLAS-SWIFT as a function of the day of year (cf. Figure 1b of the main manuscript).

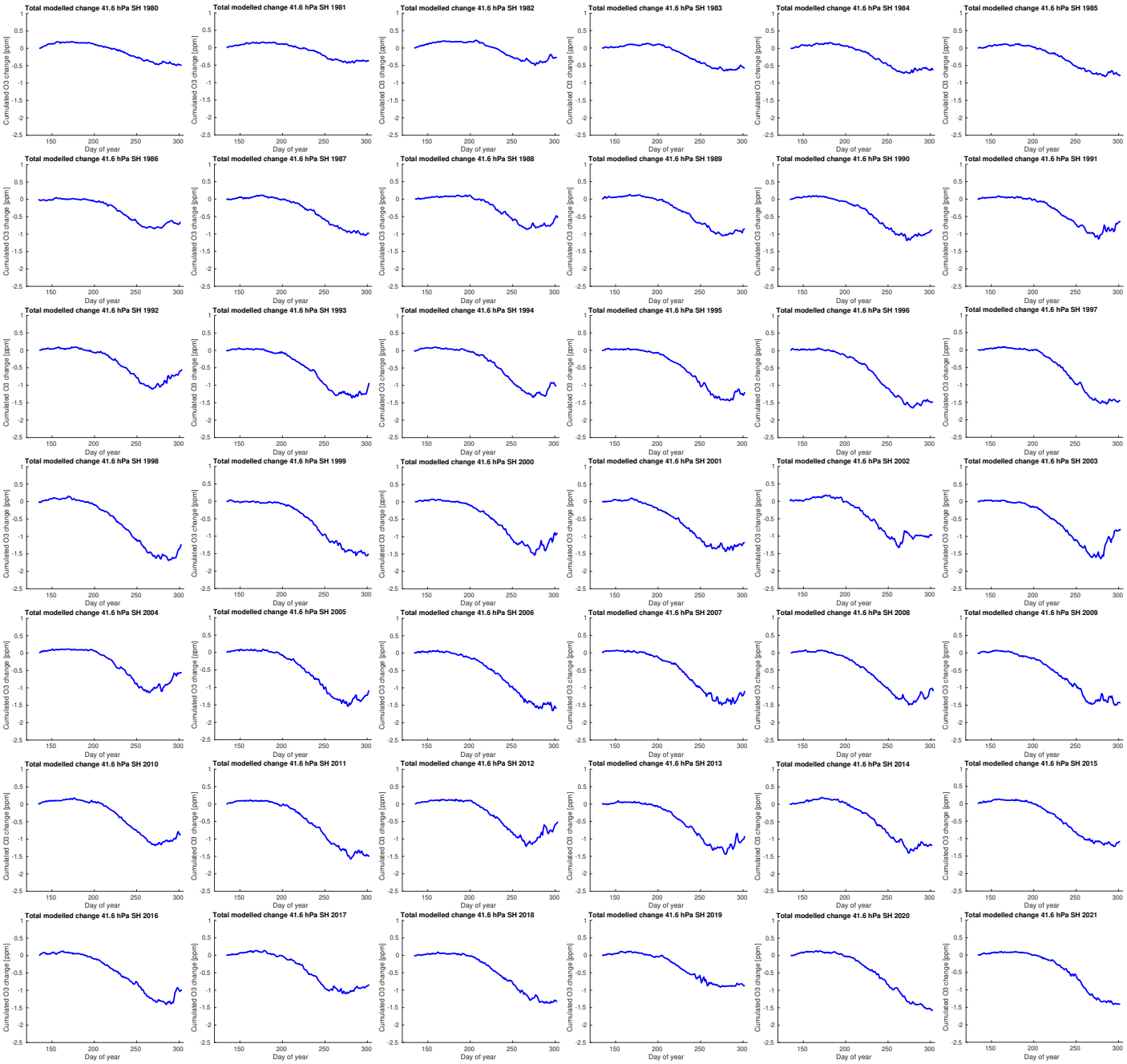

Figure S28: Cumulated total change of vortex-averaged ozone mixing ratio for the southern hemispheric winters 1980–2021 at 42 hPa (layer 3) simulated by ATLAS-SWIFT as a function of the day of year (cf. Figure 1b of the main manuscript).

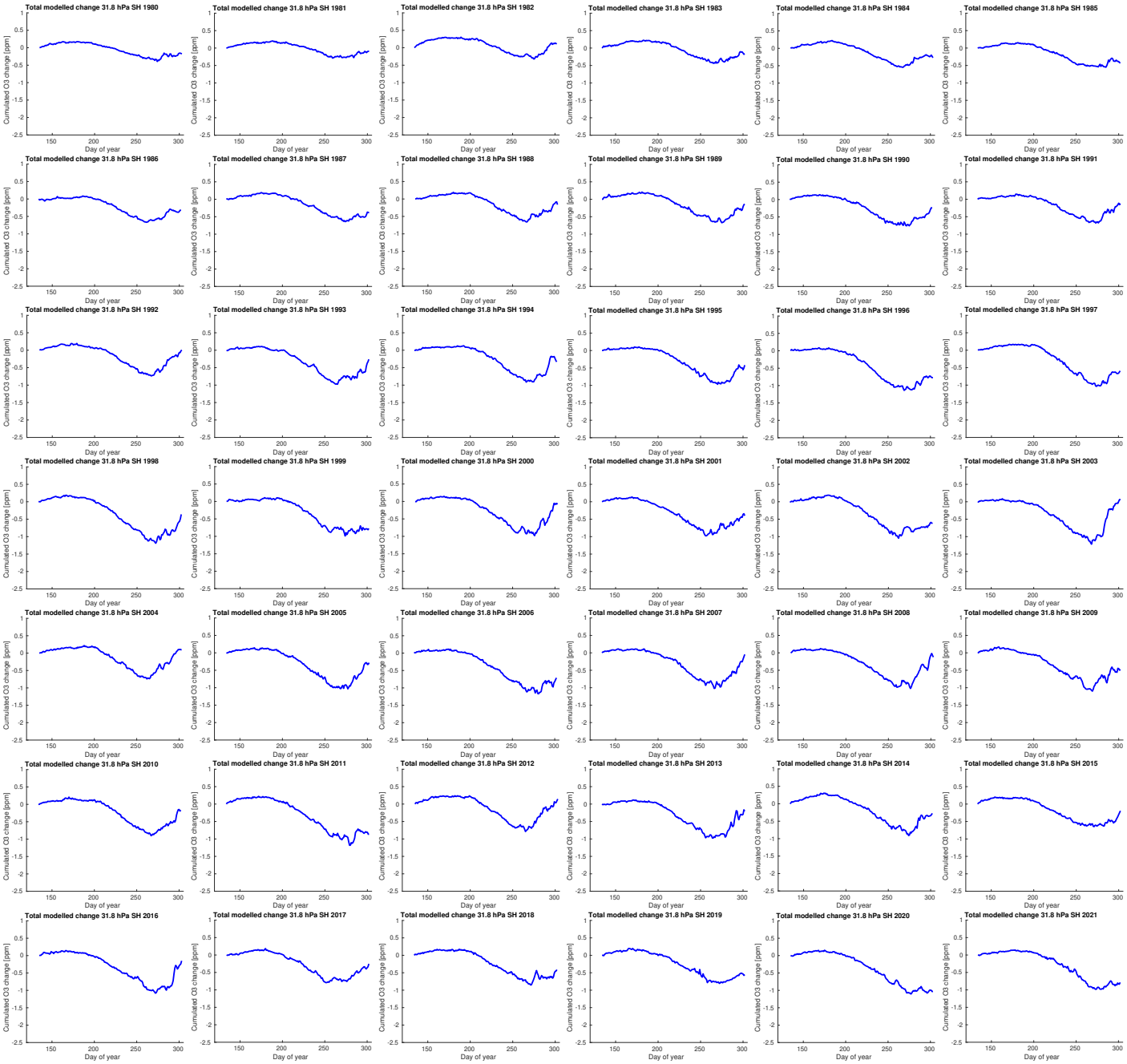

Figure S29: Cumulated total change of vortex-averaged ozone mixing ratio for the southern hemispheric winters 1980–2021 at 32 hPa (layer 4) simulated by ATLAS-SWIFT as a function of the day of year (cf. Figure 1b of the main manuscript).

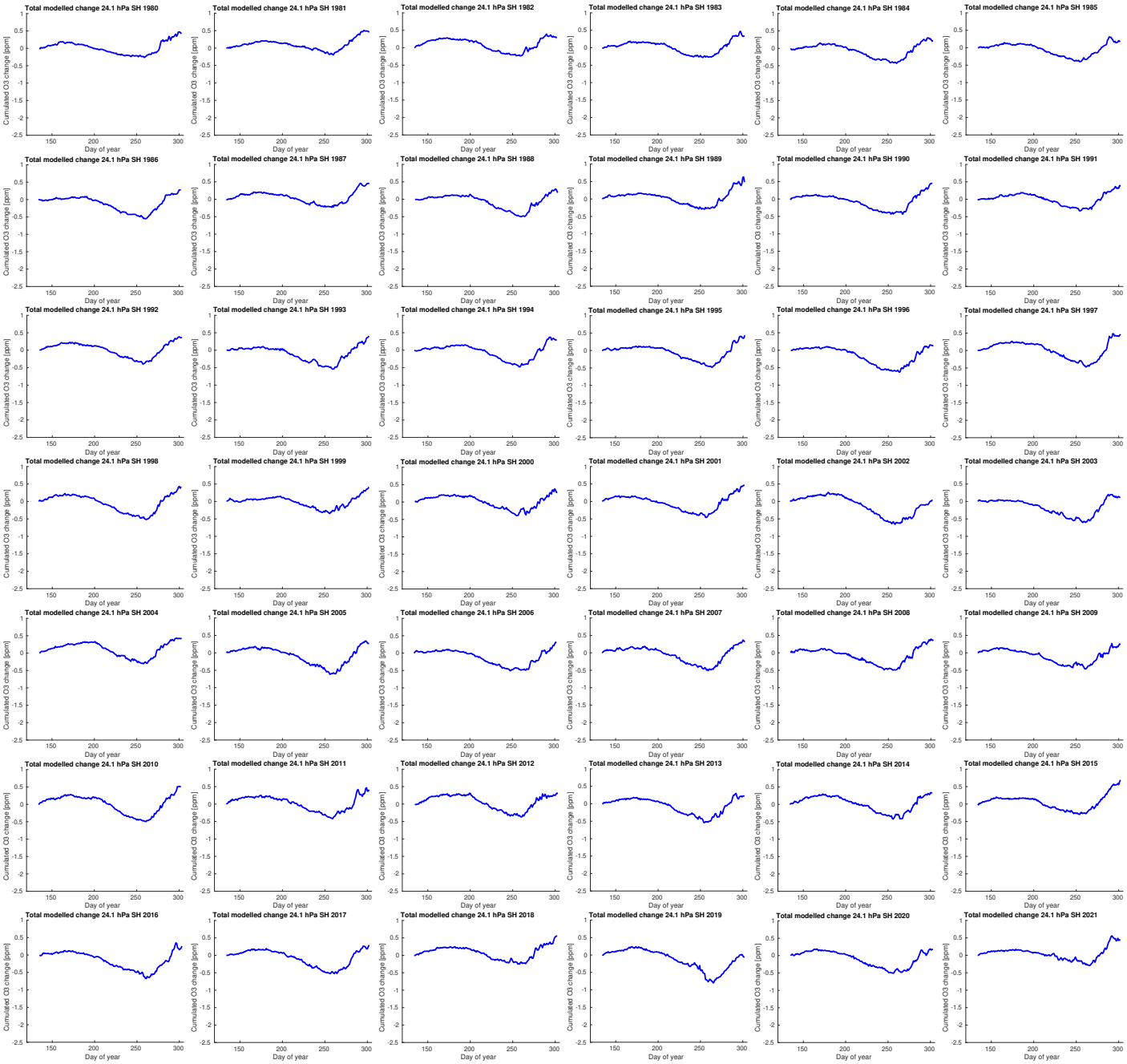

Figure S30: Cumulated total change of vortex-averaged ozone mixing ratio for the southern hemispheric winters 1980–2021 at 24 hPa (layer 5) simulated by ATLAS-SWIFT as a function of the day of year (cf. Figure 1b of the main manuscript).

11 Chemical change (southern hemisphere)

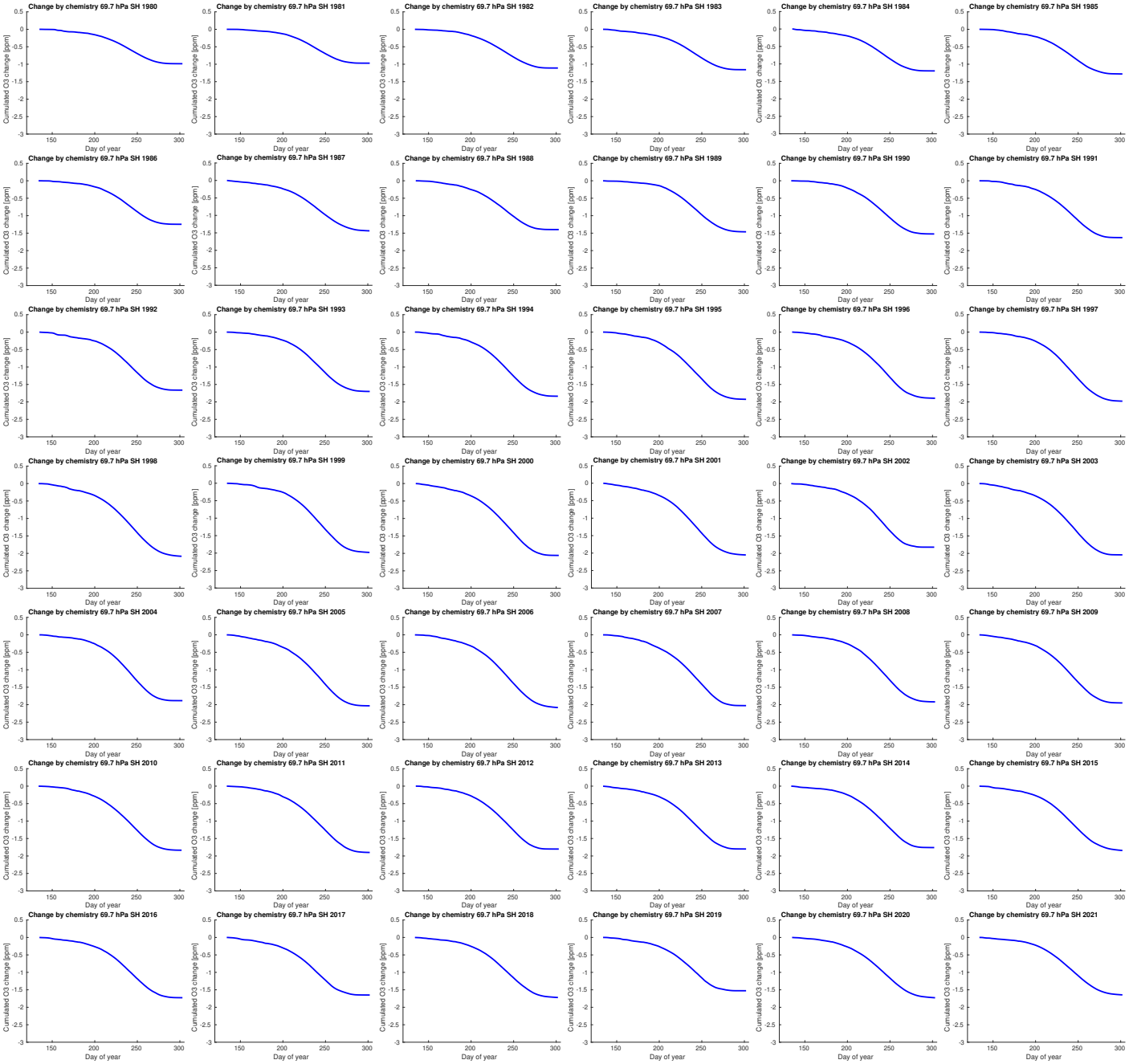

Figure S31: Cumulated change by chemistry of vortex-averaged ozone mixing ratio for the southern hemispheric winters 1980–2021 at 70 hPa (layer 1) simulated by ATLAS-SWIFT as a function of the day of year (cf. Figure 1d of the main manuscript).

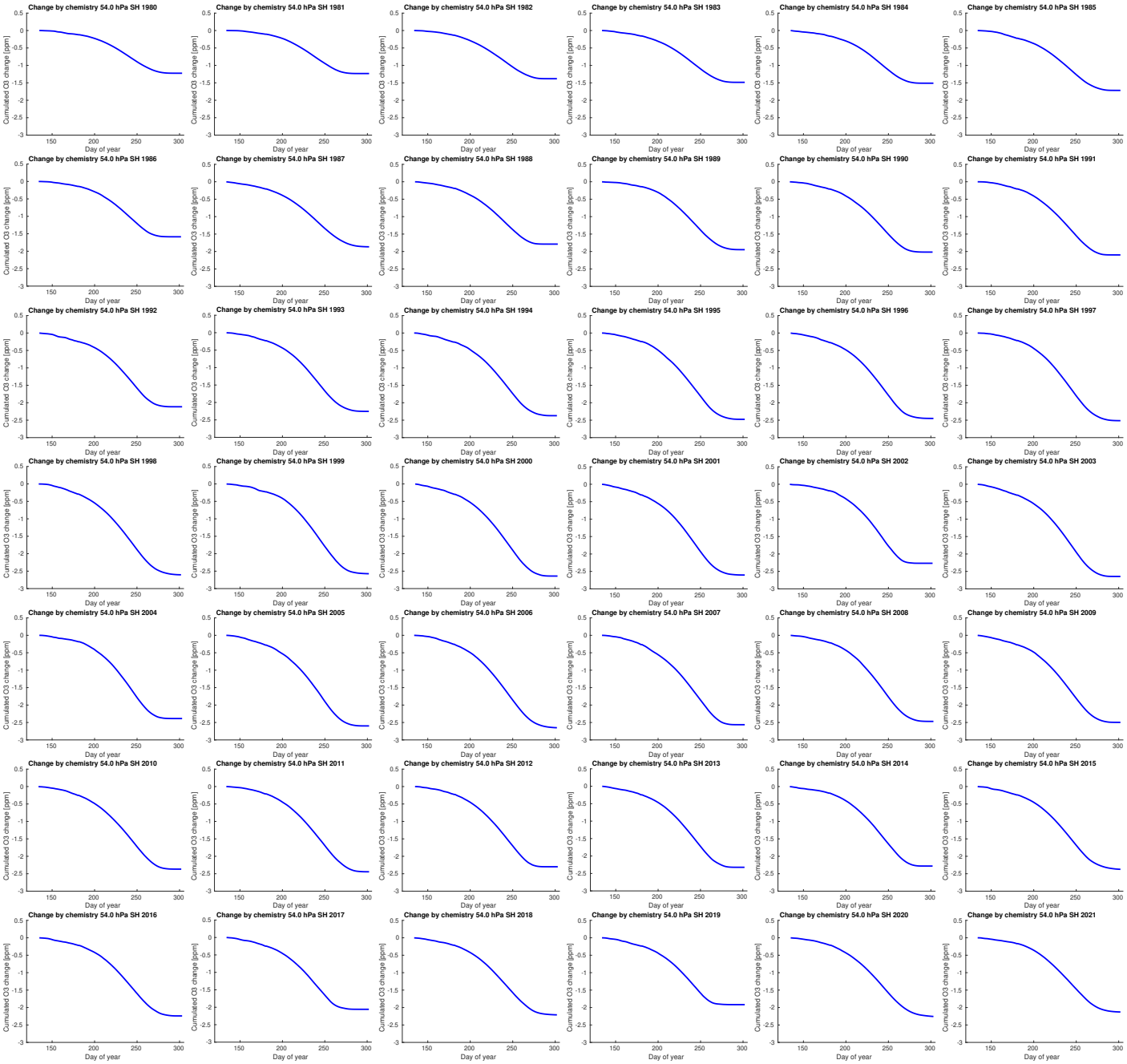

Figure S32: Cumulated change by chemistry of vortex-averaged ozone mixing ratio for the southern hemispheric winters 1980–2021 at 54 hPa (layer 2) simulated by ATLAS-SWIFT as a function of the day of year (cf. Figure 1d of the main manuscript).

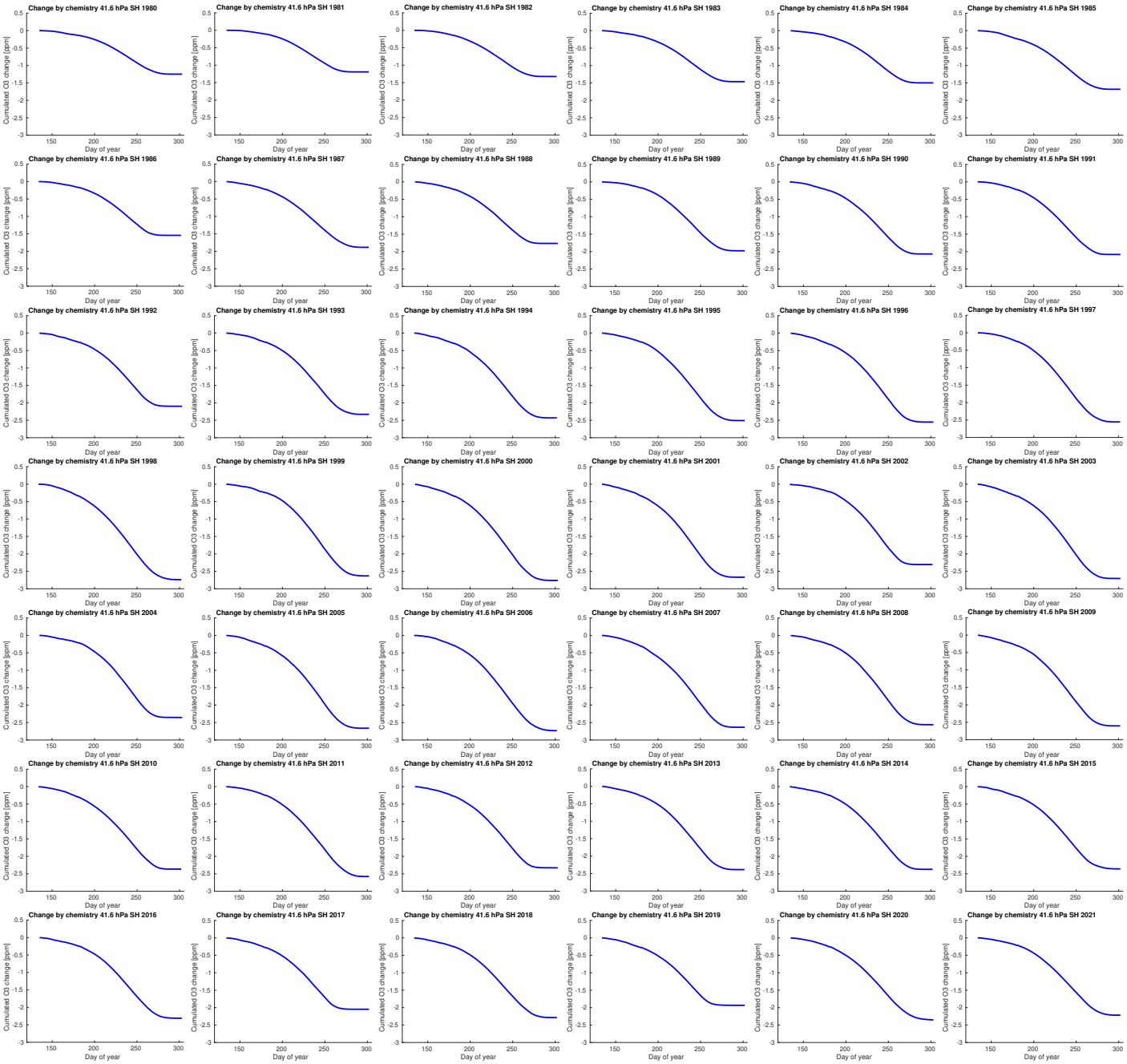

Figure S33: Cumulated change by chemistry of vortex-averaged ozone mixing ratio for the southern hemispheric winters 1980–2021 at 42 hPa (layer 3) simulated by ATLAS-SWIFT as a function of the day of year (cf. Figure 1d of the main manuscript).

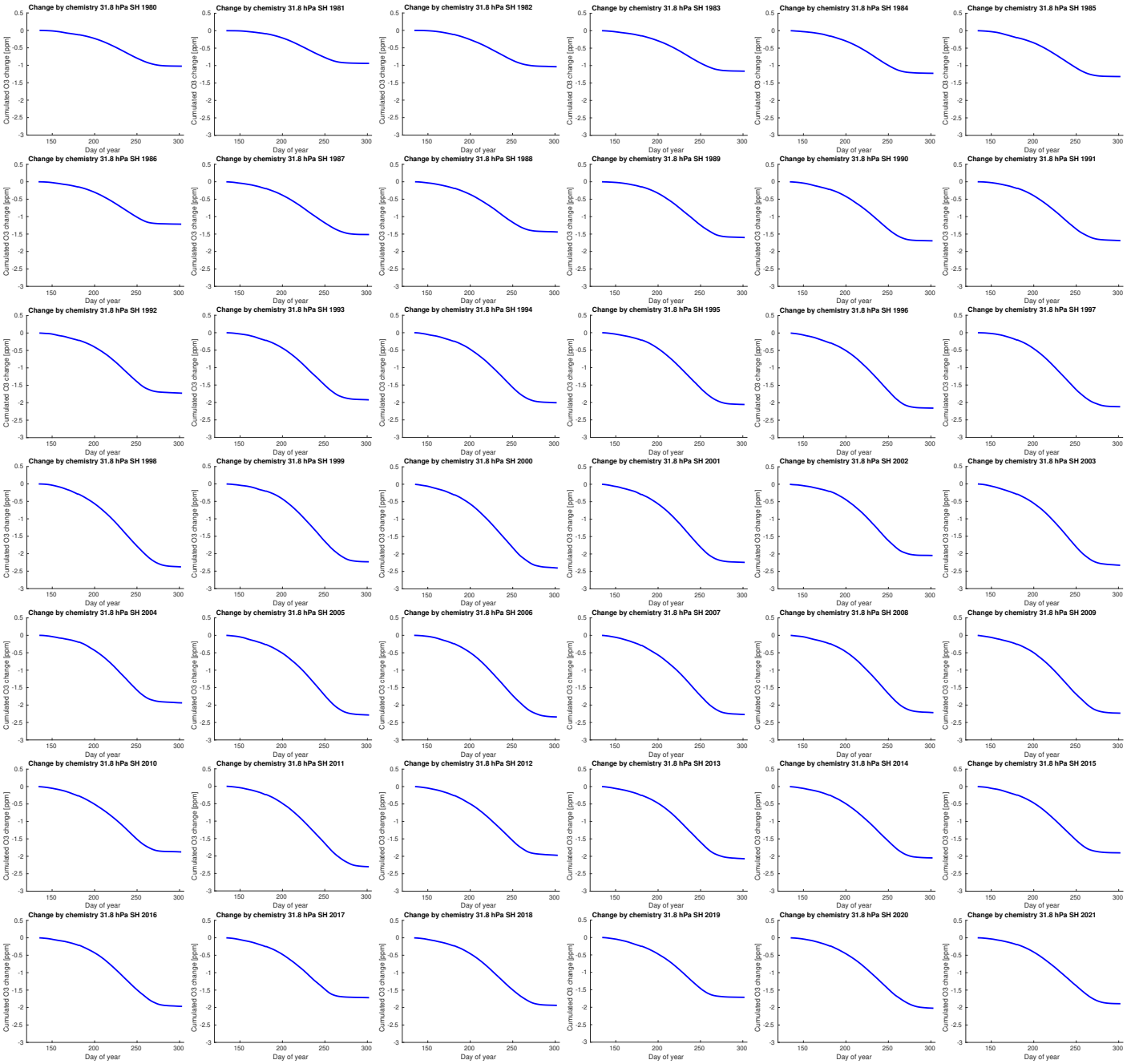

Figure S34: Cumulated change by chemistry of vortex-averaged ozone mixing ratio for the southern hemispheric winters 1980–2021 at 32 hPa (layer 4) simulated by ATLAS-SWIFT as a function of the day of year (cf. Figure 1d of the main manuscript).

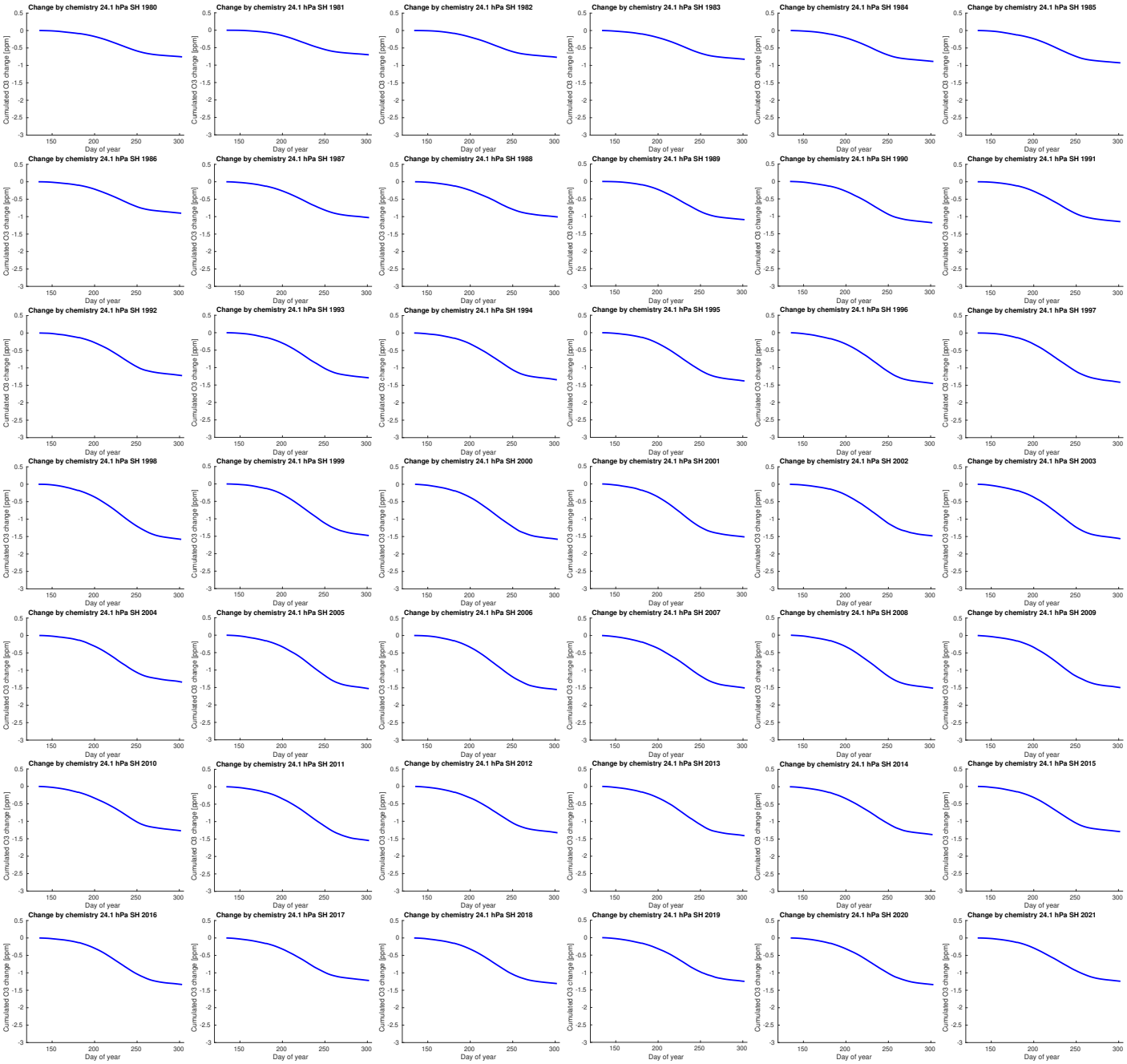

Figure S35: Cumulated change by chemistry of vortex-averaged ozone mixing ratio for the southern hemispheric winters 1980–2021 at 24 hPa (layer 5) simulated by ATLAS-SWIFT as a function of the day of year (cf. Figure 1d of the main manuscript).

12 Transport change (southern hemisphere)

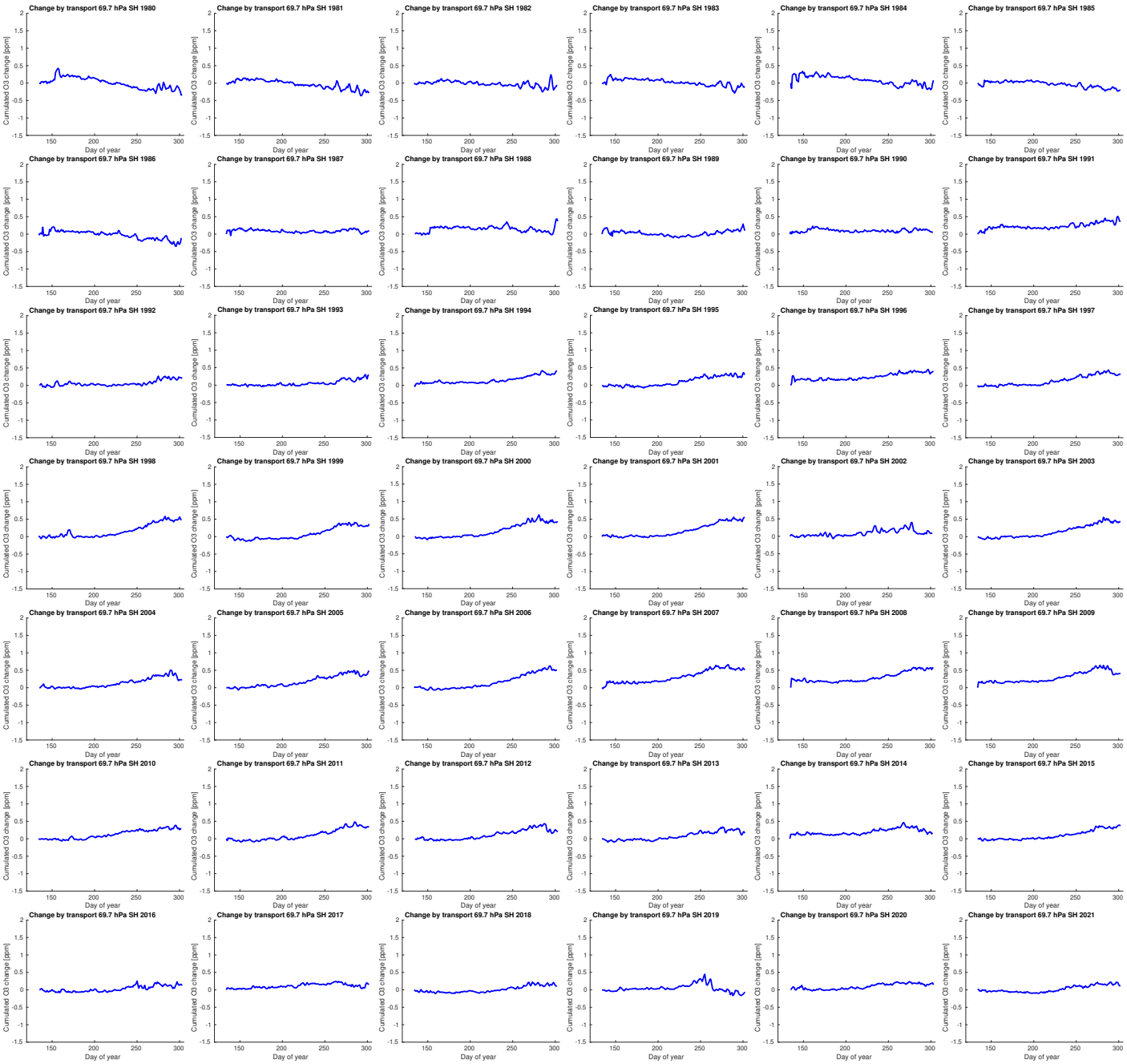

Figure S36: Cumulated change by transport of vortex-averaged ozone mixing ratio for the southern hemispheric winters 1980–2021 at 70 hPa (layer 1) simulated by ATLAS-SWIFT as a function of the day of year (cf. Figure 1f of the main manuscript).

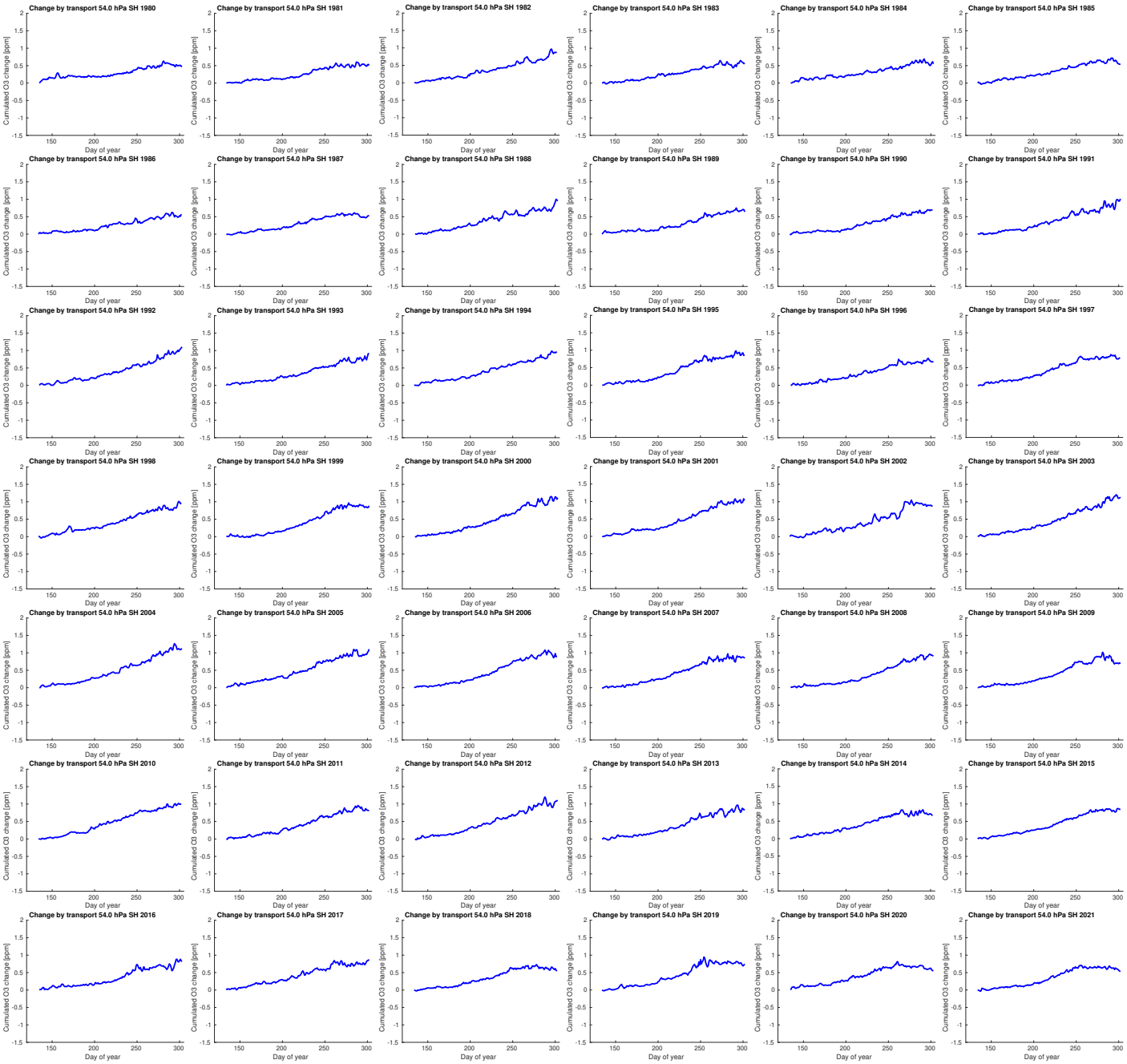

Figure S37: Cumulated change by transport of vortex-averaged ozone mixing ratio for the southern hemispheric winters 1980–2021 at 54 hPa (layer 2) simulated by ATLAS-SWIFT as a function of the day of year (cf. Figure 1f of the main manuscript).

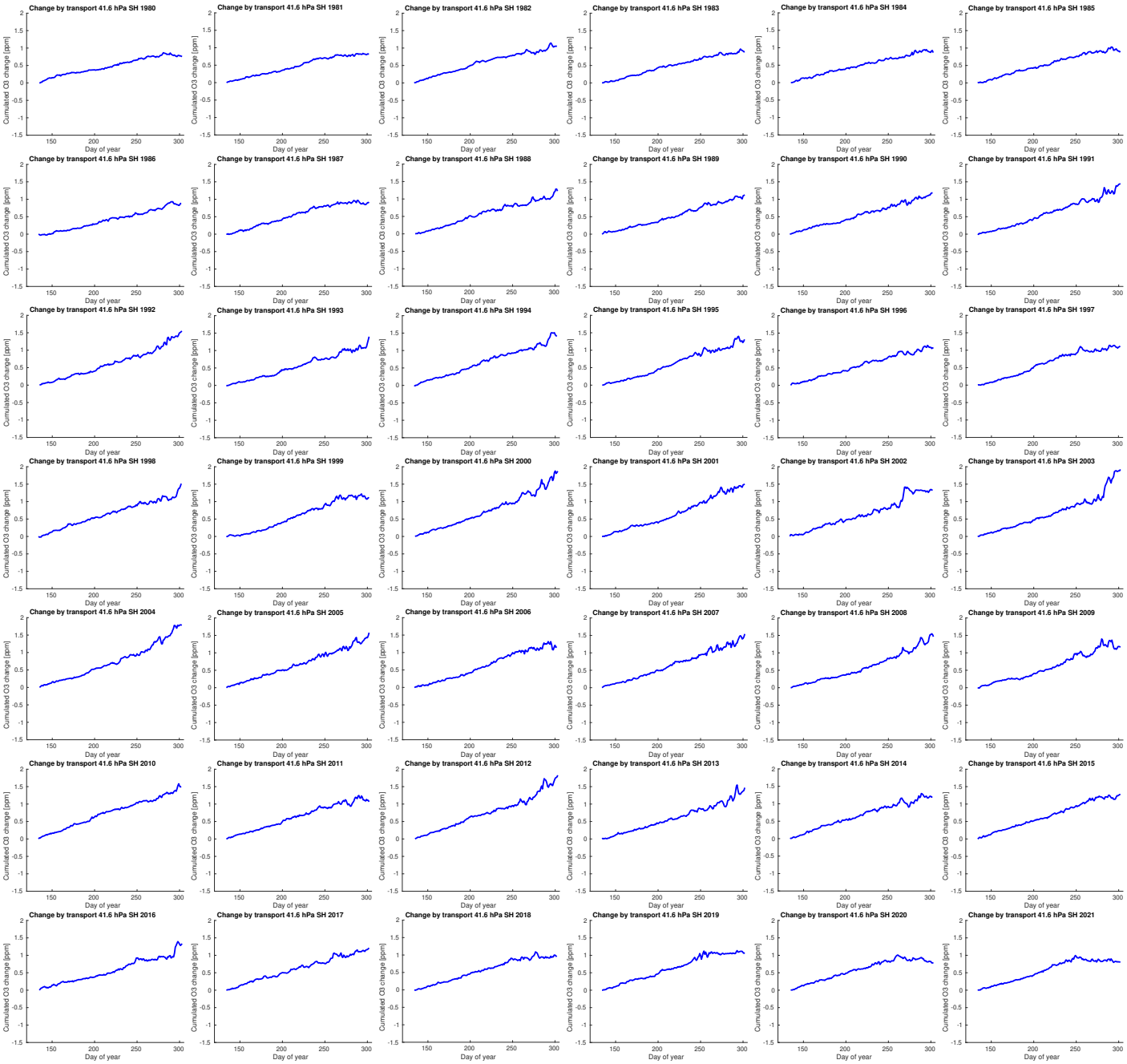

Figure S38: Cumulated change by transport of vortex-averaged ozone mixing ratio for the southern hemispheric winters 1980–2021 at 42 hPa (layer 3) simulated by ATLAS-SWIFT as a function of the day of year (cf. Figure 1f of the main manuscript).

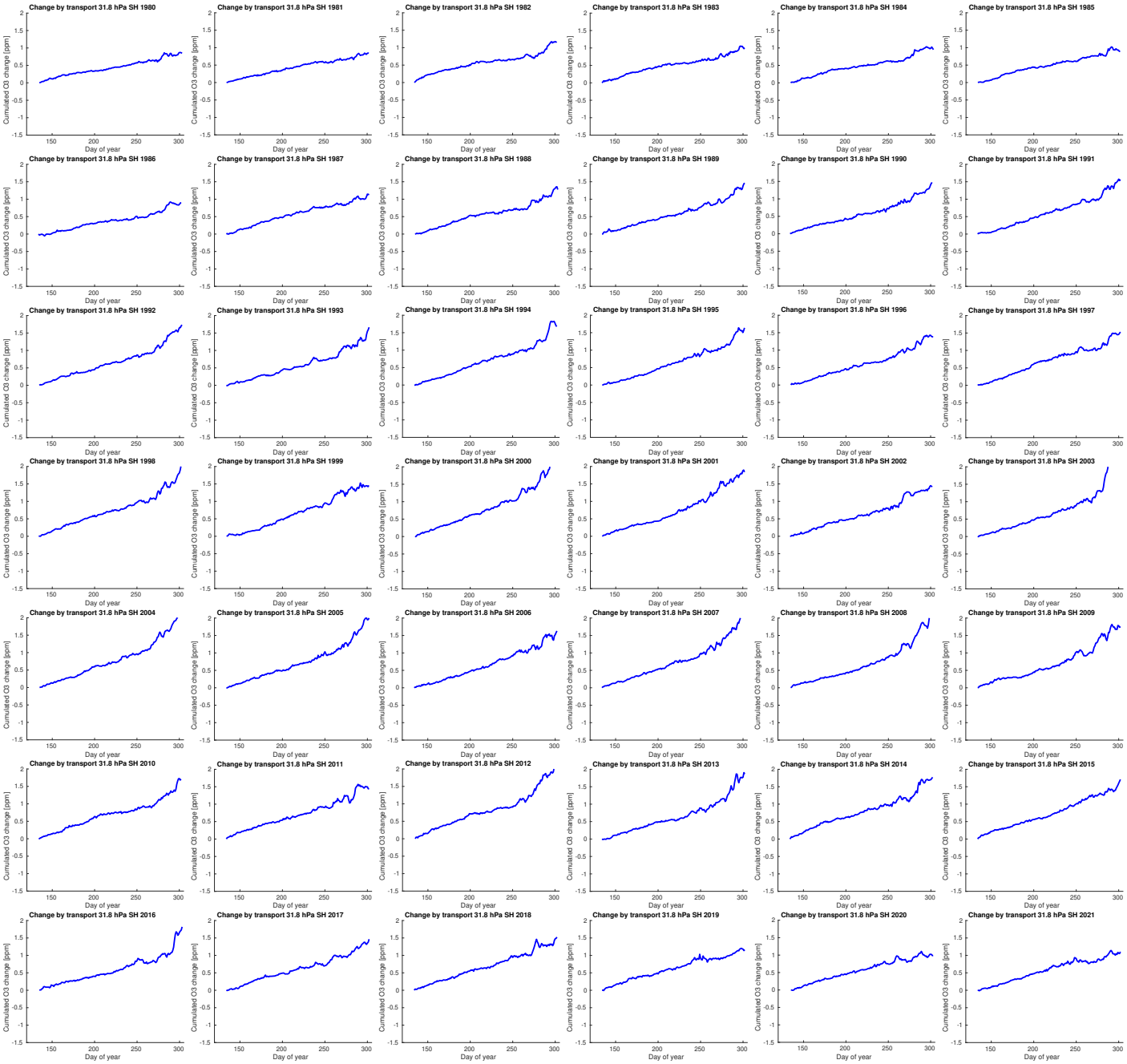

Figure S39: Cumulated change by transport of vortex-averaged ozone mixing ratio for the southern hemispheric winters 1980–2021 at 32 hPa (layer 4) simulated by ATLAS-SWIFT as a function of the day of year (cf. Figure 1f of the main manuscript).

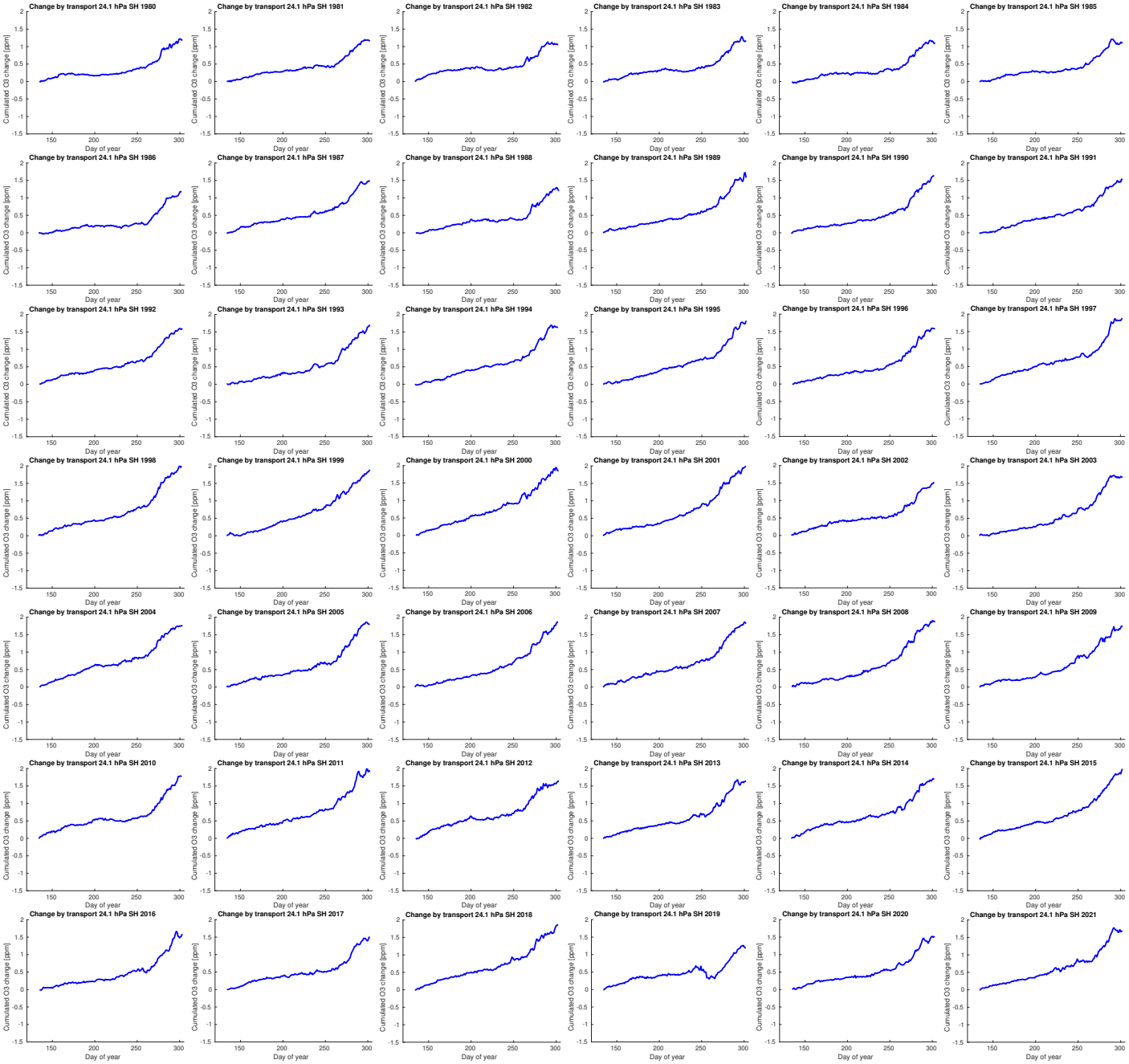

Figure S40: Cumulated change by transport of vortex-averaged ozone mixing ratio for the southern hemispheric winters 1980–2021 at 24 hPa (layer 5) simulated by ATLAS-SWIFT as a function of the day of year (cf. Figure 1f of the main manuscript).

13 Fit (southern hemisphere)

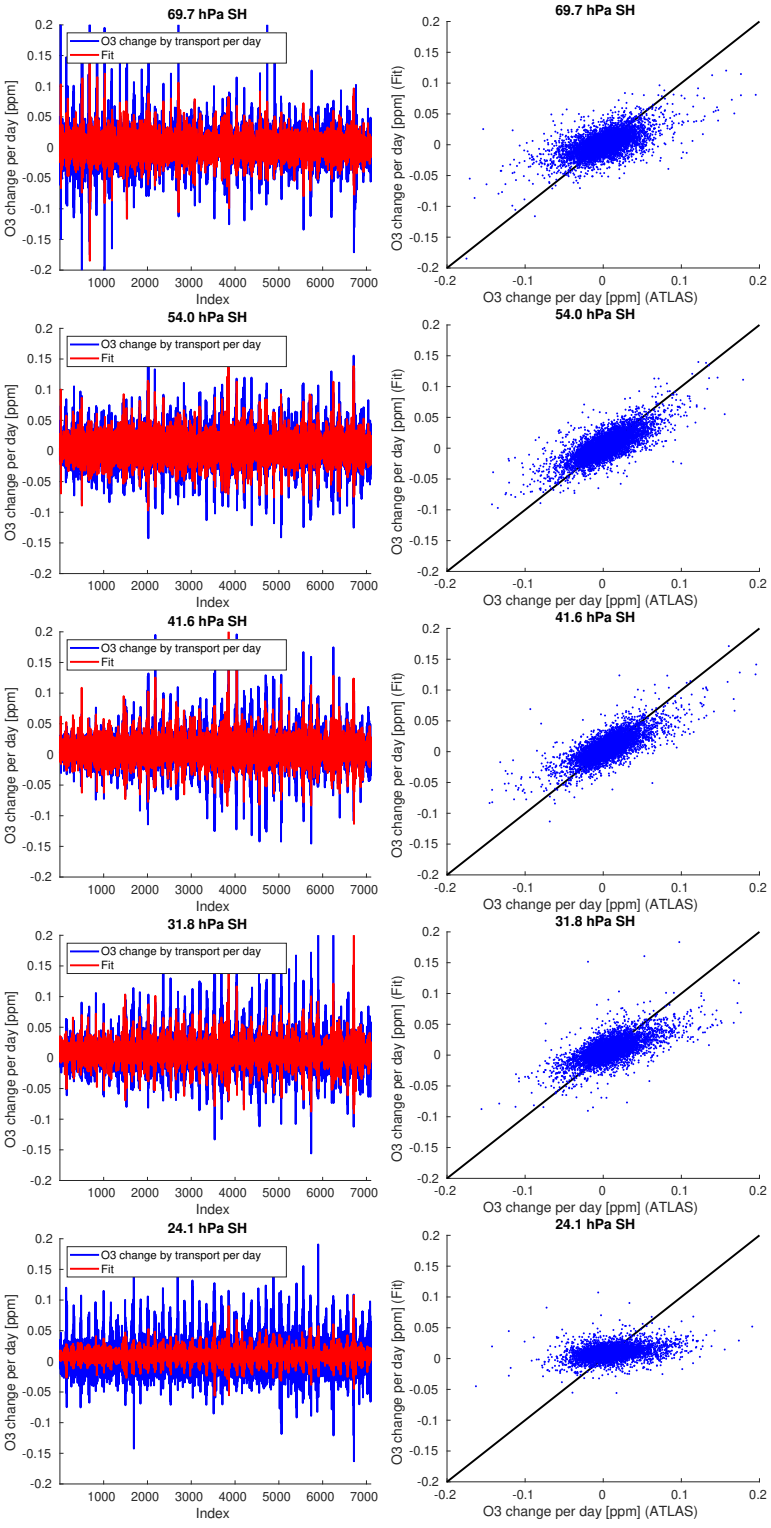

Figure S41: Left (cf. Figure 2b of the main manuscript): Concatenated time series of the change of vortex-averaged ozone mixing ratio by transport per day for all years in ATLAS-SWIFT (blue) and corresponding fit from the multivariate regression model (red). Right (cf. Figure 2d of the main manuscript): Same data as a scatter plot.

14 Vortex mean temperatures (southern hemisphere)

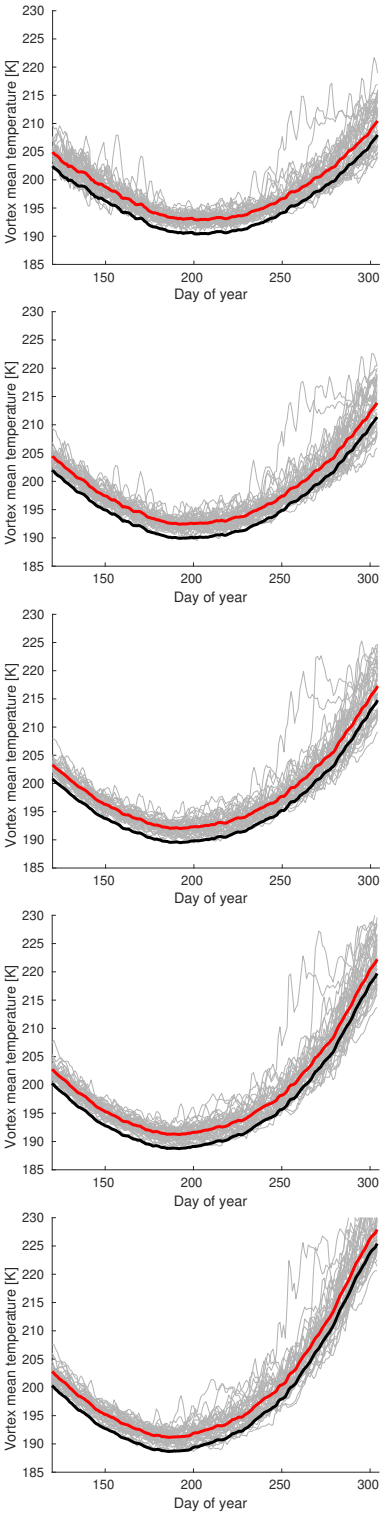

Figure S42: Vortex mean temperatures at the SWIFT levels as a function of day of year for all individual years from 1980 to 2021 based on ERA5 (grey lines), vortex mean temperature averaged over all years (red) and the same curve shifted by $-2.5\,\mathrm{K}$ as an approximation of the lower envelope of the grey lines (black) (cf. Figure 3b of the main manuscript).

15 Change of ozone versus change of temperature (southern hemisphere)

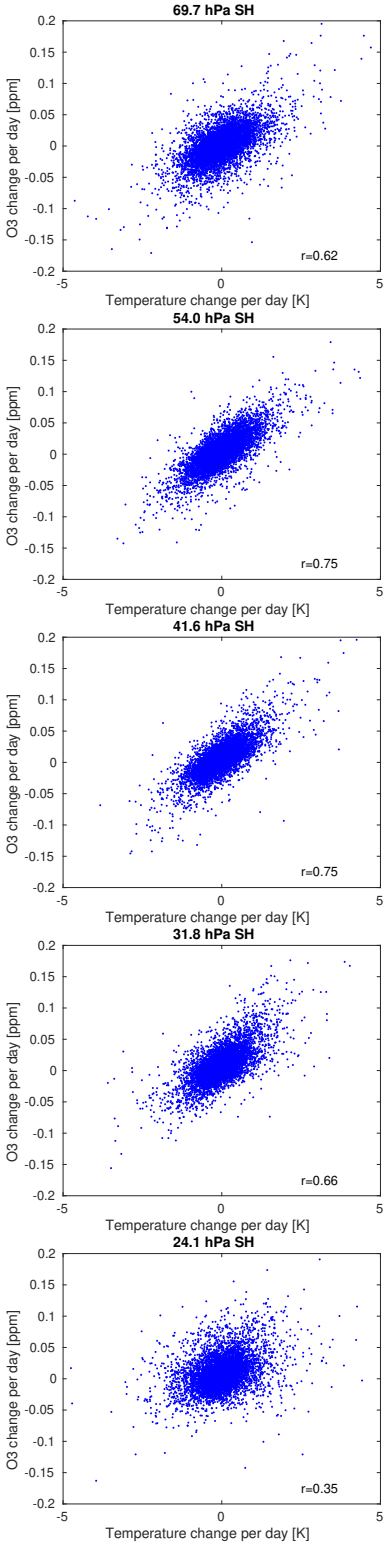

Figure S43: Scatter plot of the change of vortex-averaged ozone mixing ratio by transport per day for all years in ATLAS-SWIFT and corresponding change in vortex-averaged temperature per day, corrected for the change in radiative equilibrium temperature (cf. Figure 4b of the main manuscript).

16 Validation of the transport term (southern hemisphere)

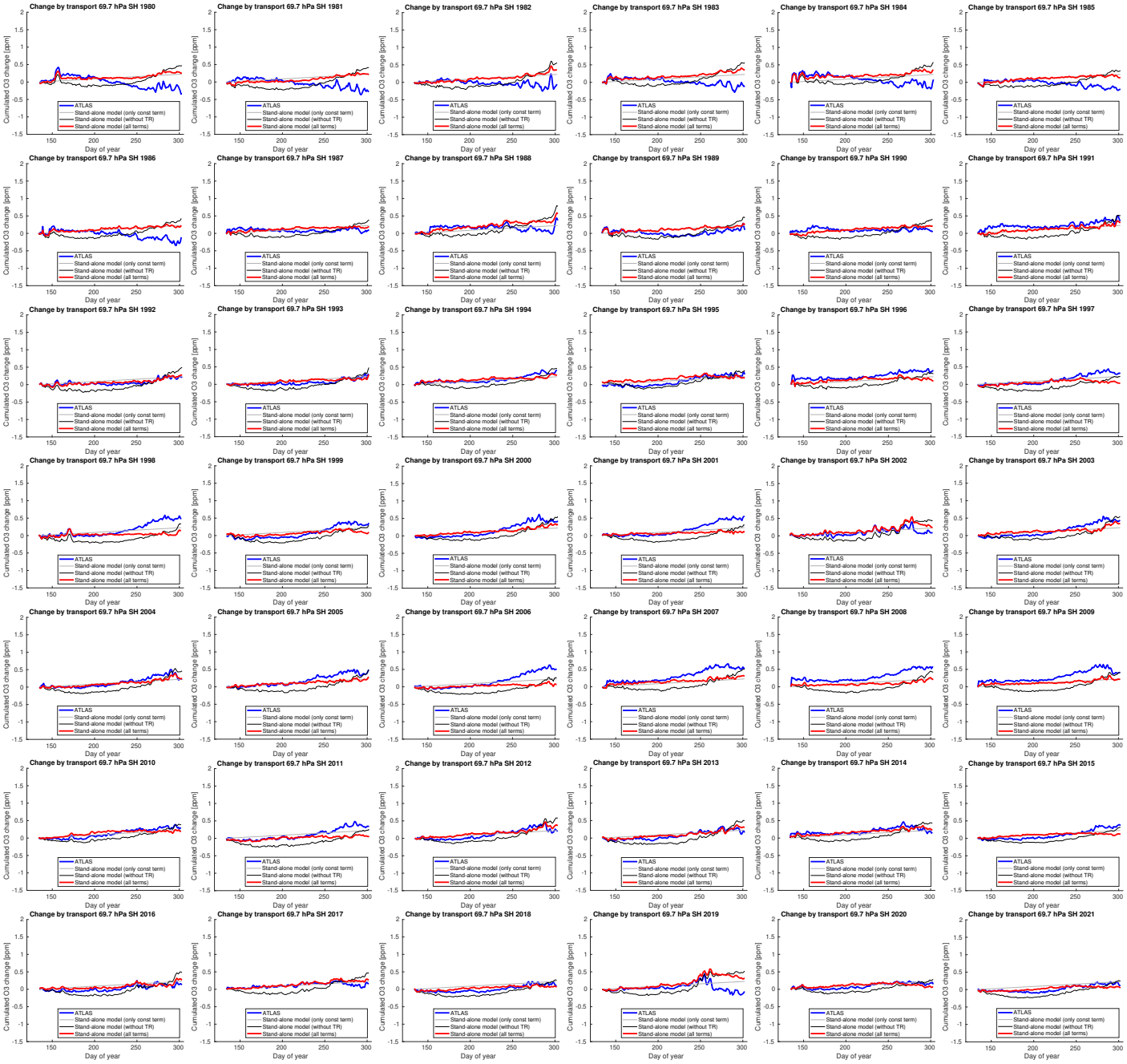

Figure S44: Cumulated vortex-averaged ozone change by transport at 70 hPa (layer 1) for the southern hemispheric winters 1980–2021 (blue) and a simulation of the cumulated change by transport by a stand-alone version of the transport parameterization (red). The thin grey line shows a simulation with only the constant term, and the thin black line shows a simulation with the constant and temperature-dependent term, but without subtracting the change of the radiative equilibrium temperature from the vortex-averaged temperature change (cf. Figure 5b of the main manuscript).

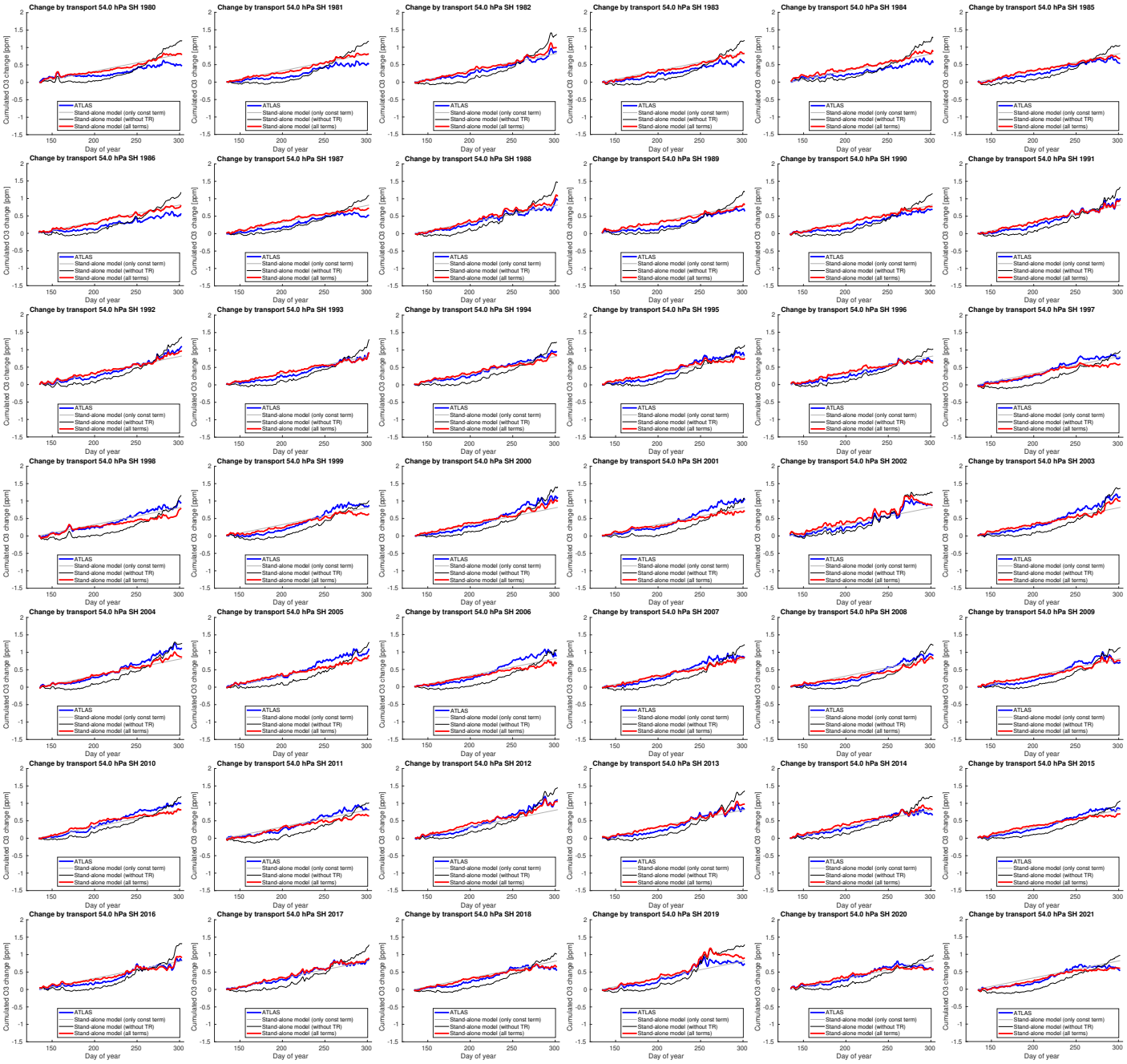

Figure S45: Cumulated vortex-averaged ozone change by transport at 54 hPa (layer 2) for the southern hemispheric winters 1980–2021 (blue) and a simulation of the cumulated change by transport by a stand-alone version of the transport parameterization (red). The thin grey line shows a simulation with only the constant term, and the thin black line shows a simulation with the constant and temperature-dependent term, but without subtracting the change of the radiative equilibrium temperature from the vortex-averaged temperature change (cf. Figure 5b of the main manuscript).

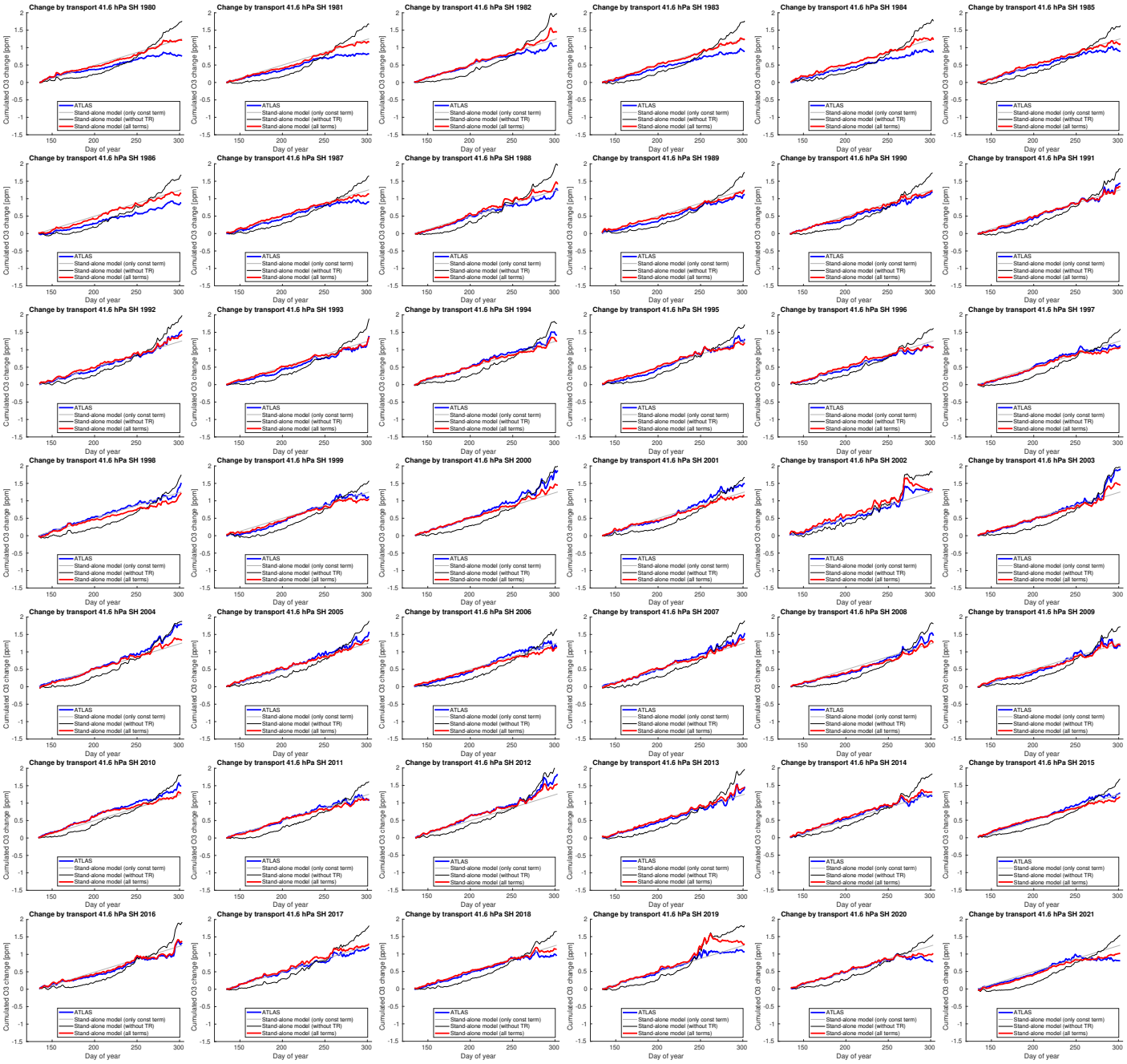

Figure S46: Cumulated vortex-averaged ozone change by transport at 42 hPa (layer 3) for the southern hemispheric winters 1980–2021 (blue) and a simulation of the cumulated change by transport by a stand-alone version of the transport parameterization (red). The thin grey line shows a simulation with only the constant term, and the thin black line shows a simulation with the constant and temperature-dependent term, but without subtracting the change of the radiative equilibrium temperature from the vortex-averaged temperature change (cf. Figure 5b of the main manuscript).

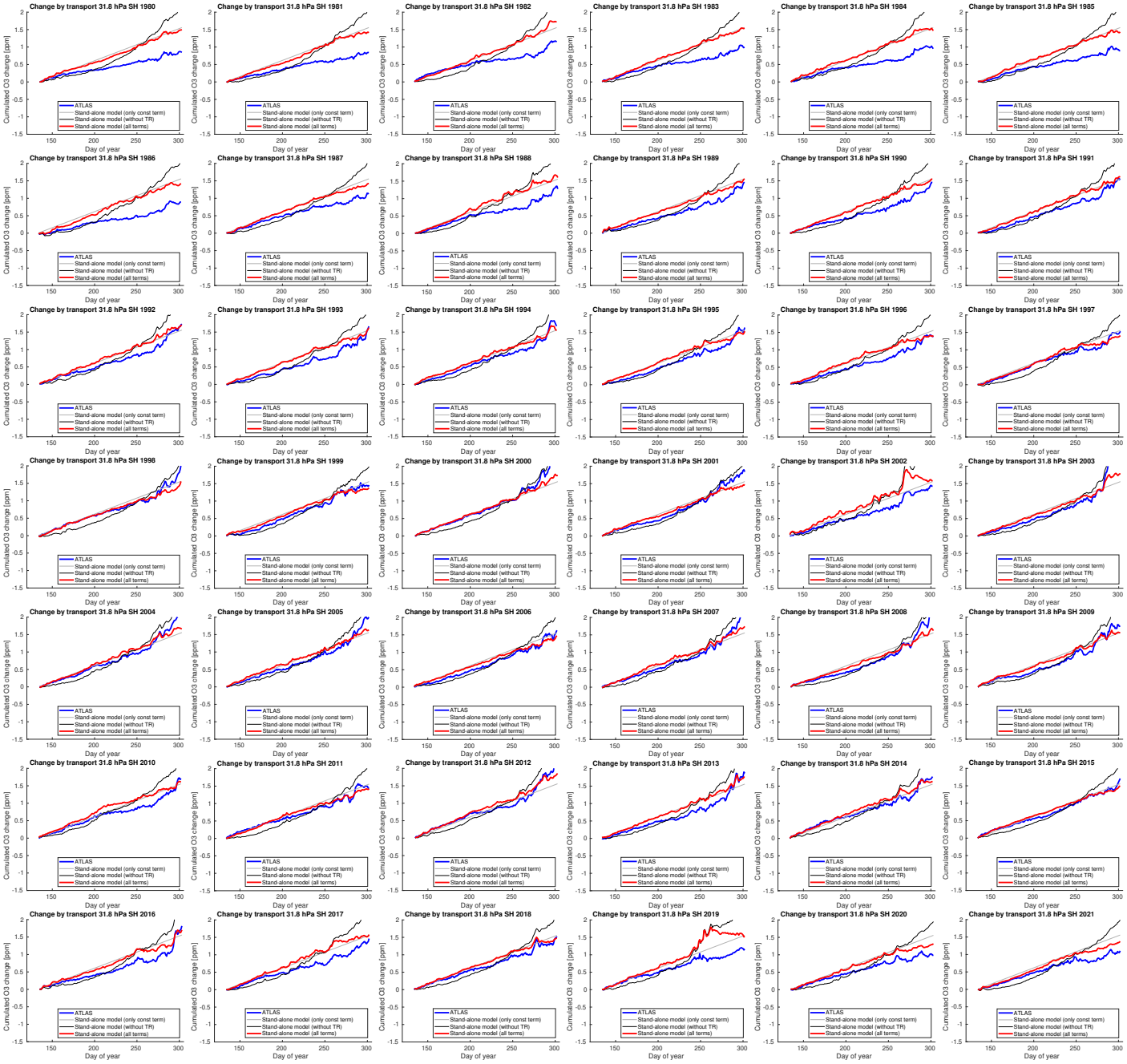

Figure S47: Cumulated vortex-averaged ozone change by transport at 32 hPa (layer 4) for the southern hemispheric winters 1980–2021 (blue) and a simulation of the cumulated change by transport by a stand-alone version of the transport parameterization (red). The thin grey line shows a simulation with only the constant term, and the thin black line shows a simulation with the constant and temperature-dependent term, but without subtracting the change of the radiative equilibrium temperature from the vortex-averaged temperature change (cf. Figure 5b of the main manuscript).

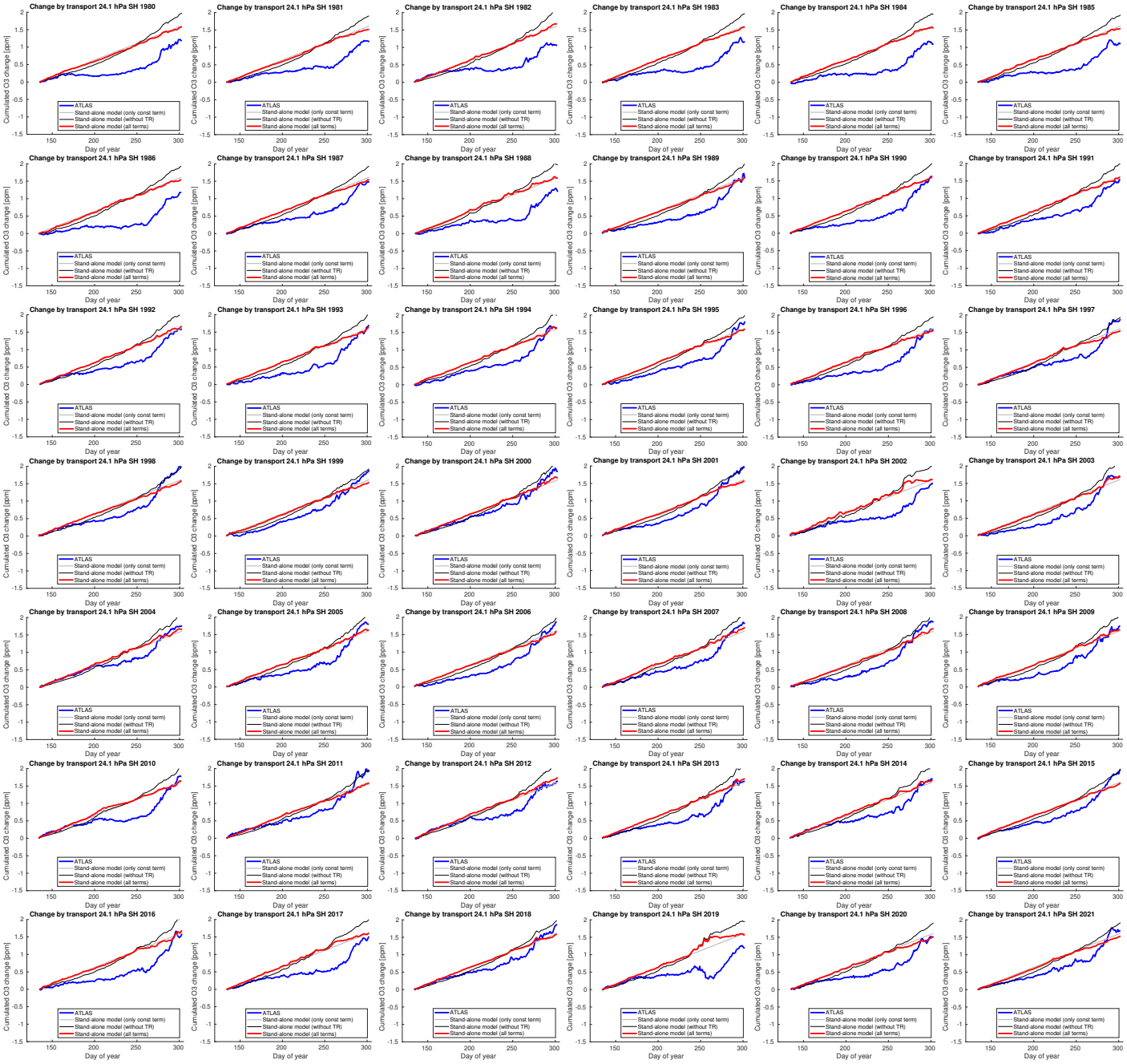

Figure S48: Cumulated vortex-averaged ozone change by transport at 24 hPa (layer 5) for the southern hemispheric winters 1980–2021 (blue) and a simulation of the cumulated change by transport by a stand-alone version of the transport parameterization (red). The thin grey line shows a simulation with only the constant term, and the thin black line shows a simulation with the constant and temperature-dependent term, but without subtracting the change of the radiative equilibrium temperature from the vortex-averaged temperature change (cf. Figure 5b of the main manuscript).

17 Validation of the complete SWIFT model (southern hemisphere)

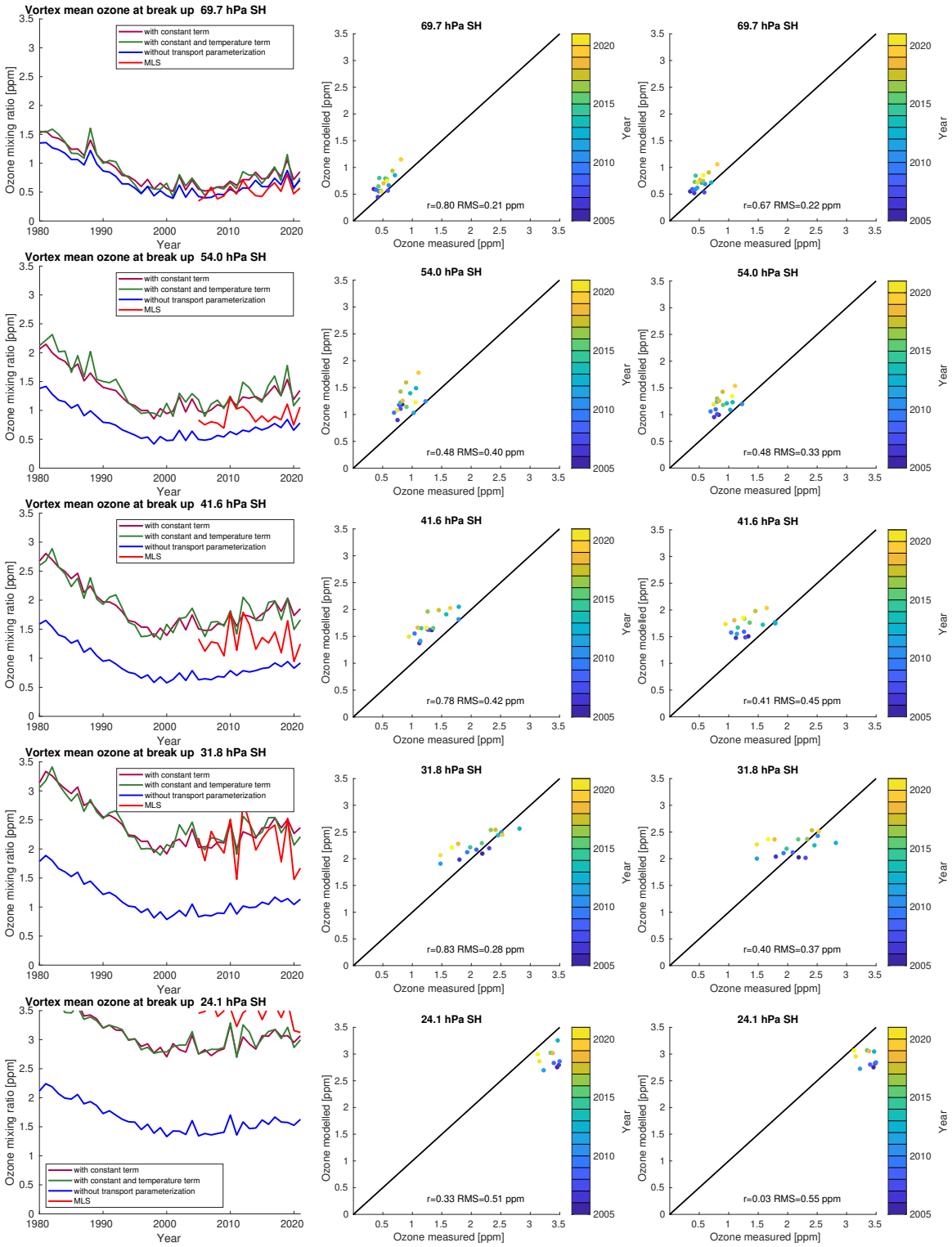

Figure S49: Left (cf. Figure 6b of the main manuscript): Vortex-averaged ozone simulated by the stand-alone Polar SWIFT model for the date of vortex breakup in the southern hemisphere for different years. Ozone mixing ratios simulated without the transport parameterization (blue), ozone mixing ratios simulated with only the "constant change" term of the transport parameterization (brown), ozone mixing ratios simulated with the full transport parameterization with the "constant change" term and temperature-dependent term (green), and corresponding measurements of ozone from the MLS instrument (red). Middle (cf. Figure 7b of the main manuscript): Scatter plot of the same data ("constant change" term and temperature-dependent term). Right: Scatter plot of the same data (only "constant change" term).

18 Difference transport term at vortex breakup of transport parameterization to ATLAS (northern hemisphere)

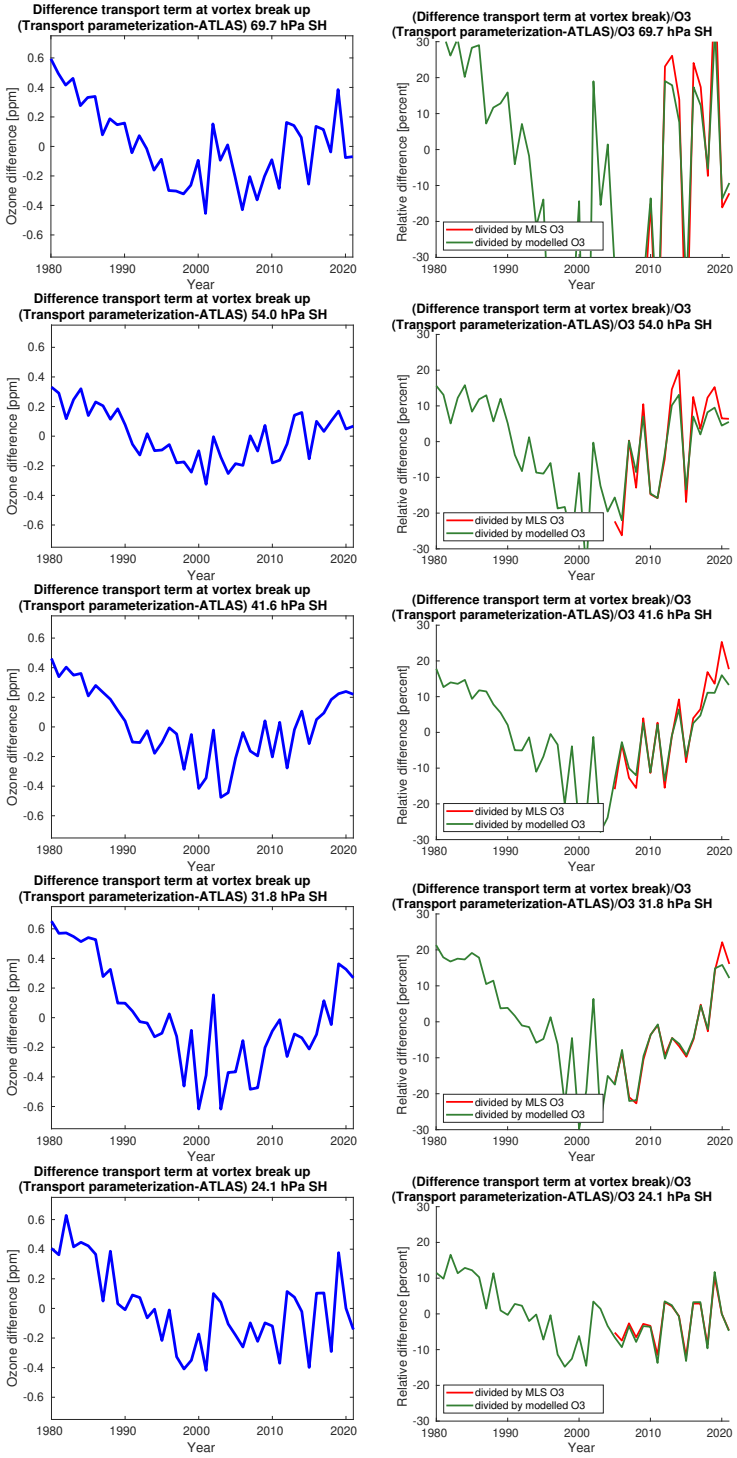

Figure S50: Left: Difference of cumulated vortex-averaged ozone change by transport at vortex break up between the transport parameterization and ATLAS-SWIFT for the southern hemispheric winters 1980–2021. Right: The difference from the left column divided by the ozone that is simulated (green) or observed by MLS (red) at this day.

19 Fit coefficients with error bars

Table S1: Fit coefficients (current version)

p [hPa]	69.66111	54.03643	41.59872	31.77399	24.07468	Unit
Constant change term NH	0.0888 ± 0.0103	0.1050 ± 0.0070	0.1068 ± 0.0084	0.0969 ± 0.0087	0.0793 ± 0.0094	$\cdot 10^{-7}\mathrm{day}^{-1}$
Constant change term SH	0.1338 ± 0.0522	0.4850 ± 0.0358	0.7423 ± 0.0345	0.9217 ± 0.0451	0.9539 ± 0.0610	$\cdot 10^{-8}\mathrm{day}^{-1}$
Temperature-dependent term NH	0.2814 ± 0.0095	0.2841 ± 0.0063	0.2221 ± 0.0072	0.1489 ± 0.0073	0.0579 ± 0.0072	$\cdot 10^{-7}\mathrm{K}^{-1}$
Temperature-dependent term SH	0.2533 ± 0.0075	0.3097 ± 0.0060	0.3152 ± 0.0061	0.2775 ± 0.0074	0.1375 ± 0.0086	$\cdot 10^{-7}\mathrm{K}^{-1}$